POLITECNICO
MILANO 1863

SCUOLA DI INGEGNERIA INDUSTRIALE
E DELL'INFORMAZIONE

Study on NV-center stability in diamond nanoparticles for quantum information science applications

Tesi di Laurea Magistrale in
Nuclear Engineering

Author: **Francesco Martinelli**

Student ID: 990442
Advisor: Prof. David Dellasega
Co-advisors: Prof. Giulia Galli, Dr. Arpan Kundu
Academic Year: 2022-23

Abstract

This thesis presents computational modeling of nitrogen vacancy (NV) centers in diamondoids for applications in quantum information science. Density functional theory calculations are exploited to investigate the electronic structure of NV centers embedded in nanodiamonds with varying surface terminations, starting from the standard hydrogen-terminated diamondoids. A key finding is that the fluorine terminated nanodiamond has a favorable electronic structure, with the two NV-empty levels sufficiently below the conduction band of diamond and the vacuum level, making it well suitable for Quantum Information Science (QIS) applications.
The effect of embedding NV-nanodiamonds within molecular crystals and applying pressure is also analyzed. Pressure is responsible for inducing quantum confinement effects that increase the gap between defect levels and the conduction band, guaranteeing a better accommodation for the NV-levels that reside within the gap.
Lastly, the electron-phonon coupling is explored to understand the impact of the temperature on the system, which is found to be negligible even at room-temperature, confirming the system promise in the QIS context.
Overall, this work provides insights into engineering NV-nanodiamonds through surface chemistry and external pressure to optimize their quantum properties, paving the way for their integration into practical quantum devices.

Keywords: NV-center, Diamondoids, Molecular Crystals, DFT

Abstract in lingua italiana

Questa tesi si pone come obiettivo primario presentare i risultati della modellazione computazionale di diamantoidi in cui sono stati impiantati dei Nitrogen Vacancy (NV) centers, con lo scopo di valutare la possibilità di impiegarli come qubit in hardware quantistici.
La Teoria del Funzionale della Densità (DFT) viene utilizzata per esplorare la struttura elettronica di questi particolari sistemi.
L'analisi inizia dai diamantoidi terminati con atomi di idrogeno e si estende alle nanostrutture con diverse terminazioni superficiali. In particolare, le nanoparticelle terminate con atomi di fluoro si rivelano adatte agli scopi preposti, in quanto la struttura elettronica necessaria per l'impiego degli NV-center come qubit viene completata, con i due stati vuoti che si collocano al di sotto della banda di conduzione e della soglia di vuoto.
Il lavoro comprende anche un'analisi sull'impatto di pressione e temperatura quando i diamantoidi cristallizzano in cristalli molecolari.
La pressione gioca un ruolo determinante nell'indurre effetti di confinamento quantistico, aumentando il gap tra la banda di conduzione e i livelli del difetto, assicurando un migliore accomodamento per questi ultimi.
L'effetto della temperatura viene introdotto tramite lo studio dell'interazione tra elettroni e fononi, che si rivela essere ininfluente anche a temperatura ambiente.
Questa ricerca fornisce una linea guida per l'ingegnerizzazione di sistemi che utilizzano gli NV-center come qubit all'interno di diamantoidi, esplorando la possibilità di funzionalizzare la superficie di queste nanostrutture e di applicare pressioni elevate alla loro fase cristallina, con il fine di ottimizzarne le proprietà elettroniche. Tale approccio apre la strada all'integrazione di questi sistemi in dispositivi quantistici relizzabili.

Keywords: NV-center, Diamantoidi, Cristalli Molecolari, Teoria del Funzionale della Densità (DFT)

Contents

[1]This chapter has been developed within the context of the Honours Programme "Scientific Research in Industrial Engineering".

1 | Introduction to Quantum Computation and Molecular Qubits

In the modern era of scientific and technological advancements, the exploration and understanding of complex systems have become fundamental to tackle the most challenging engineering problems. From climate modeling to plasma simulations, from neutronic modeling in fission reactors to interfacial chemical reaction studies, diverse research fields have the common requirement of obtaining robust solutions to complex problems. Central to this pursuit is the relentless demand for computational power, which continues to escalate as the intricacy of the systems under investigation deepens.
In the quest for deeper insights and more accurate predictions, researchers have increasingly turned to computational methods to simulate and model the behavior of complex systems. However, as the complexity of these systems rises, so too do the computational resources required to simulate their behavior, ultimately reaching the limits of conventional classical computing architectures.

The domain of quantum computing, an area that holds immense promise for revolutionizing the landscape of computation-intensive tasks, could be the solution to this need.
For instance, quantum algorithms have been proposed for simulating complex plasma phenomena like turbulence and transport in fusion reactors [26].
These algorithms can efficiently represent the behavior of plasma particles and calculate their time evolution through different techniques, granting the possibility to model plasma dynamics and instabilities with unprecedented accuracy, since the actual Particle-In-a-Cell (PIC) codes scales exponentially with the number of macro-particles that are simulated, making impossible to estimate behaviors of a significant number of particles.

In the realm of nuclear physics, quantum computing methods have demonstrated potential for precisely calculating properties of atomic nuclei using lattice quantum chromodynamics, underlining the necessity of improved quantum hardware to scale up the complexity of analyzed nuclei [50].
Moreover, quantum algorithms offer a unique avenue to address complex challenges in this domain, with applications that culminate in simulating nuclear fission processes to optimize reactor design.
For example, random processes involved in nuclear fission simulations are actually based on classical Monte Carlo methods, which rely on the generation of random numbers, that are not actually random, since they are generated following any type of logic. On the other hand, quantum random number generation exploits the intrinsic randomness of quantum processes, which could be fundamental to improving the simulations of neutron propagation and their role in inducing fission reactions, thereby improving reactor design. The synergy between complex system simulations and quantum computing forms the cornerstone of a new era in computational science, where quantum advantages may soon be realized for tackling computationally demanding problems across scientific domains.

Nonetheless, the current state of quantum computing is not without its challenges. Despite remarkable advances in hardware development and algorithmic innovation, quantum computers still show issues of stability, error correction, and scalability. These limitations restrain the optimism surrounding quantum computing's potential.

Quantum computing appears as a ray of hope, providing a fascinating look into a future in which complicated problems are solved in the world of the quantum. However, the road to realize this promise is full of stumbling blocks that necessitate a comprehensive knowledge of both theoretical foundations and practical limits.

1.1. Quantum Computation in a Nutshell

Before delving into the details of this work it is necessary a bit of context, especially on the general framework in which the aim of this thesis is developed, so all the basic concepts, that push the scientists to direct their efforts toward the development of quantum computers, have to be understood.

Quantum computation is a revolutionary paradigm in computer science that harnesses

the principles of quantum mechanics to perform calculations that would be practically impossible or extremely time-consuming using classical computers.
At its core, quantum computing uses quantum bits, or qubits, to represent and manipulate the information. Unlike classical bits, which can only be in a state of 0 or 1, qubits can exist in a superposition of both 0 and 1 simultaneously.

A single qubit can be implemented using various physical systems, such as electrons' spin or the polarization of photons.
The key feature of a qubit is its ability to exist in a linear combination of its basis states, denoted as $|0\rangle$ and $|1\rangle$, so, mathematically, a qubit's state can be represented as $|\psi\rangle = \alpha|0\rangle + \beta|1\rangle$, where α and β are complex numbers satisfying $|\alpha|^2 + |\beta|^2 = 1$, and it can be pictured on a Bloch sphere (in figure 1.1).

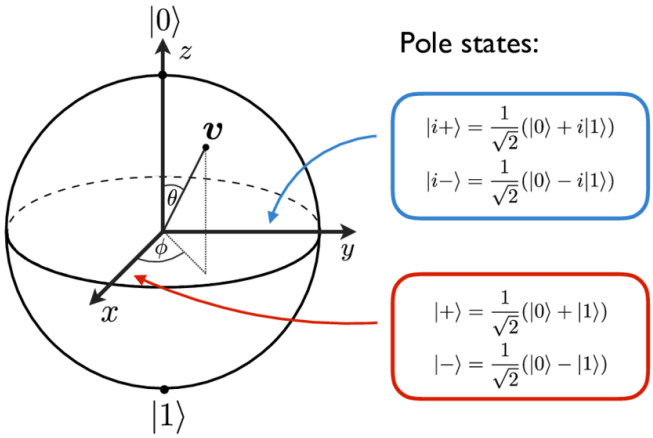

Figure 1.1: Qubit representation on the Bloch sphere [28]

1.1.1. Qubit Manipulation

In classical computation, to build any algorithm it is necessary to manipulate the information stored in the memory, and this is accomplished through the logical gates: AND, OR, NOT, NOR, XNOR, XOR, and NAND.
In quantum computation, qubits are manipulated using quantum gates, which can be represented as unitary operators that act on the quantum state of the qubits.
Each quantum gate performs specific operations, such as changing the qubit's state (e.g. Pauli-X gate, Pauli-Y gate, Pauli-Z gate, Hadamard gate) or entangling multiple qubits (e.g. CNOT gate), and it can be visualized as a rotation on the Bloch sphere.

Pauli Gates

The Pauli-X gate, often referred to as the X gate, is a fundamental quantum gate that performs a bit-flip operation on a qubit. It maps the state $|0\rangle$ to $|1\rangle$ and $|1\rangle$ to $|0\rangle$. Mathematically, the X gate can be represented as follows:

$$X = \begin{bmatrix} 0 & 1 \\ 1 & 0 \end{bmatrix} \tag{1.1}$$

The effect of gate application on a qubit can be represented on the Bloch sphere as a π-rotation around the x-axis.
In the same flavor the Y gate and the Z gate can be represented on the Bloch sphere as a π-rotation respectively around the y-axis and the z-axis.

$$Y = \begin{bmatrix} 1 & 0 \\ 0 & -1 \end{bmatrix}, \quad Z = \begin{bmatrix} 0 & -i \\ i & 0 \end{bmatrix} \tag{1.2}$$

Hadamard Gate

The Hadamard gate, denoted as H, is a fundamental gate used for creating superposition states. It transforms a qubit's state as follows:

$$H|0\rangle = \frac{1}{\sqrt{2}}(|0\rangle + |1\rangle), \quad H|1\rangle = \frac{1}{\sqrt{2}}(|0\rangle - |1\rangle). \tag{1.3}$$

The Hadamard gate maps the basis states to an equal superposition, making it a crucial component of many quantum algorithms.

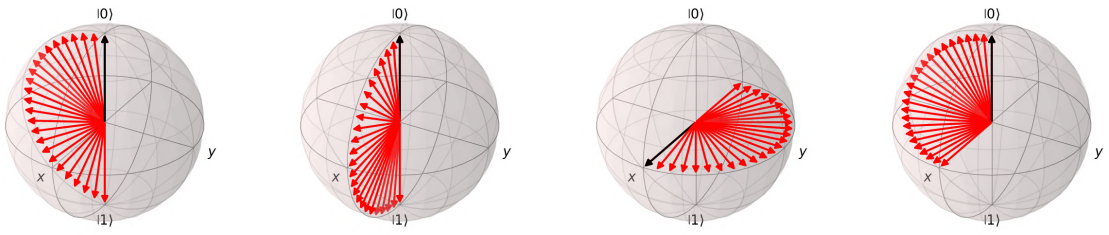

(a) X-Gate applied to $|0\rangle$ state.

(b) Y-Gate applied to $|0\rangle$ state.

(c) Z-Gate applied to $\frac{1}{\sqrt{2}}|0\rangle + \frac{1}{\sqrt{2}}|1\rangle$ state.

(d) H-Gate applied to $|0\rangle$ state.

Figure 1.2: Single qubit gates representations on the Bloch sphere (computed with QuTiP[24]).

CNOT Gate

The Controlled-NOT (CNOT) gate is a two-qubit gate that performs a controlled bit-flip operation.
It has two inputs: a control qubit and a target qubit and if the control qubit is in state $|1\rangle$, it applies the Pauli-X gate to the target qubit; otherwise, it doesn't interact with the target qubit. Mathematically, the CNOT gate is represented as:

$$\begin{aligned} \text{CNOT}(|0\rangle \otimes |\psi\rangle) &= |0\rangle \otimes |\psi\rangle, \\ \text{CNOT}(|1\rangle \otimes |\psi\rangle) &= |1\rangle \otimes X|\psi\rangle. \end{aligned} \tag{1.4}$$

$$\text{CNOT} = \begin{bmatrix} 1 & 0 & 0 & 0 \\ 0 & 1 & 0 & 0 \\ 0 & 0 & 0 & 1 \\ 0 & 0 & 1 & 0 \end{bmatrix} \tag{1.5}$$

The CNOT gate plays a crucial role in creating entanglement between qubits.

These are just some examples of the quantum gates used in quantum computation there are many more gates with specific functions and properties that are essential for constructing quantum circuits and implementing quantum algorithms.

1.1.2. DiVincenzo Criteria

Now that the building blocks of quantum computation have been established it is important to understand when it is possible to build a quantum computer, and this is accomplished through the DiVincenzo criteria's fulfillment.
The DiVincenzo Criteria [12], named after the physicist David P. DiVincenzo, serve as a roadmap for the development and evaluation of quantum hardware and software:

1. **A scalable physical system with qubits:** To build a useful quantum computer, one must choose a physical platform that can support a sufficient number of qubits while maintaining their quality. Scalability is crucial to solve complex problems.

2. **The ability to initialize qubits:** Quantum algorithms often start from a known initial state. Therefore, a practical quantum computer must be able to prepare qubits in the desired initial state with high accuracy.

3. **Long qubit coherence times:** Quantum information is fragile and can be easily disrupted by environmental factors. For practical computation, qubits must maintain their coherence (quantum information) for sufficiently long periods to allow for complex computations.
4. **Universal quantum gates:** A quantum computer should have a set of universal quantum gates that can be used to perform any arbitrary quantum operations on qubits. These gates, operated with specific physical interactions with the system, enable the implementation of quantum algorithms efficiently.
5. **A reliable qubit-state readout:** To obtain the results of quantum computations, there must be a reliable method for reading the final state of qubits accurately.

1.1.3. Quantum Algorithms: Building the Quantum Supremacy

All the properties that have been cited allow quantum computers to explore multiple solutions to a problem in parallel, potentially making them exponentially faster for certain tasks.
Although it is necessary to build proper algorithms for each task to exploit all the potential of these machines.
In this moment, the speed-up has been already tested on simple algorithms that allow to solve NP-hard problems that, by definition, require an exponential increase of time with the enlargement of the system: algorithms like Shor's algorithm for integer factorization and Grover's algorithm for unstructured search guarantee exponential speedup over classical counterparts [18, 47], threatening the security of widely-used encryption schemes and offering new possibilities in optimization.

1.1.4. Quantum Computing Platforms

Once the theory is fixed, it is important to focus on an exploration of the multifaceted field of quantum computer realization, that provides a comprehensive foundation for the ensuing discussions and analyses.

Superconducting qubits, minute circuits crafted from superconducting materials, are leading the race in practical quantum computing. Operating at near absolute zero temperatures, they exploit their quantum behavior. Noteworthy, pioneers like IBM, Google, and Rigetti have showcased their quantum supremacy, surmounting classical capabilities, and

actively focusing on upscaling for practical applications. For example in 2019 the Google Sycamore processor (in figure 1.3) has completed in 200 s a task that would have taken 10000 years on a classical computer. [5]

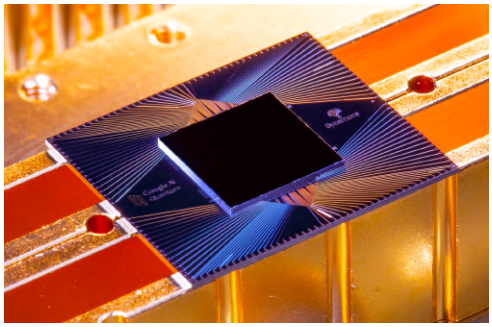

Figure 1.3: Google Sycamore superconducting processor.

In a trapped ion hardware, individual ions are manipulated via precisely controlled electromagnetic fields, as can be seen in the schematic figure 1.4, the ions are held in an electromagnetic trap, in which they are controlled with lasers or microwaves. External control and internal Coulomb coupling allow the exploitation of a set of universal quantum gates [9]. Pioneering companies like IonQ and Honeywell have achieved exceptional control, reducing errors and enhancing quantum gate precision. These systems hold a promise for error-corrected quantum computing, quantum simulations, and quantum cryptography.

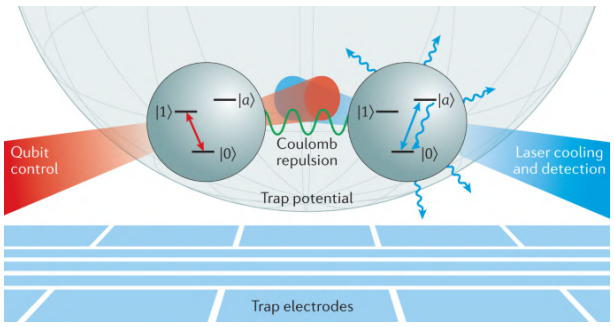

Figure 1.4: Trapped ion qubit typical configuration.

Another extremely fascinating approach is being investigated within Microsoft's Station Q project, which explores topological qubits, to increase robustness against environmental noise. These qubits leverage the unique properties of topological quantum systems to create fault-tolerant quantum states. Though still in the experimental phase, topological

qubits offer a potential solution to some of the most challenging obstacles in quantum computing since they exploit the topological protection of information stored in the processor.

Photonic qubits use photons to encode and process quantum information. Companies like PsiQuantum have embarked on the development of photonic quantum computers, emphasizing their potential for secure quantum communication and quantum simulations. Although these systems harness the inherent speed and low error rates of photons, in case of good isolation from the environment, they need incredibly precise detectors and instrumentation to manipulate the circuits.

While not as scalable as some other technologies, NMR qubits have their place in quantum computing research. They use principles of nuclear magnetic resonance to encode and manipulate quantum information. NMR-based quantum computers are valuable for exploring quantum algorithms and basic quantum principles in controlled environments.

A particularly useful quantum architecture for some classes of problems is the quantum annealer, a specialized quantum processor designed for solving optimization problems. D-Wave, a pioneer in this field, has developed quantum annealing systems that leverage quantum tunneling and adiabatic evolution to find optimal solutions to complex problems in various domains, including finance and logistics. This architecture for these reasons is completely different with respect to gate-based quantum computation.

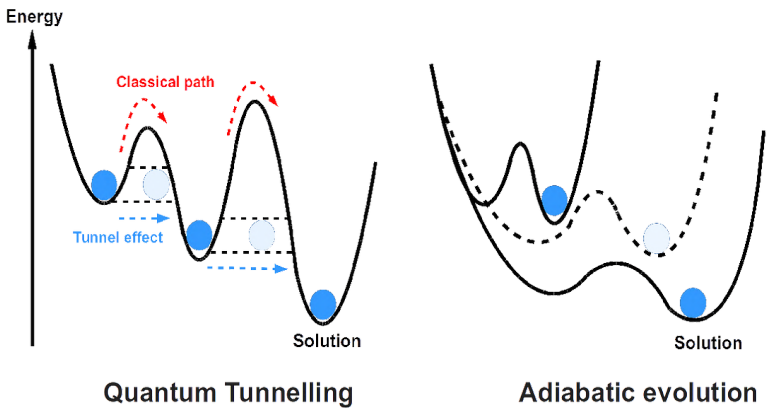

Figure 1.5: Quantum annealing process and adiabatic evolution of a system.

Among the previously mentioned companies, Intel is a notable player in the development

of silicon spin qubits, one of the most promising types of solid-state qubits. These qubits use the spin of individual electrons in silicon-based devices. Leveraging existing semiconductor fabrication technology, silicon spin qubits have the potential for scalability and integration with classical computing systems.

Another emerging trend in quantum computing is the development of hybrid quantum systems, which combine different quantum technologies to harness the strengths of multiple approaches. This approach aims to overcome some of the limitations of individual qubit types, potentially paving the way for more robust and versatile quantum computers.

Within all these possibilities, molecular qubits are promising as well, thanks to their surprising tunability in the design phase of the single molecules. This allows to exploit the electronic structure of these molecules to encode quantum information. Moreover, they could be extremely reliable and versatile due to the possibility of integrating them in different systems. For example, it has been demonstrated that chromium (IV)-based molecular qubits in a non-isostructural host matrix are non-sensitive to noise, producing long coherence time [6]. This paves the way for the development of engineered systems in which molecular qubits coupled with a proper environment could demonstrate huge reliability and scalability. Additionally, some molecular qubits can operate at or near room temperature, potentially reducing hardware complexity and costs.
On the other hand, the effort to find the perfect molecule design and correct coupling with the environment could take a lot of time, due to the intrinsically infinite possibility in system exploration.

The state of the art in quantum computer realization is a dynamic landscape, characterized by intense research and innovation across various experimental platforms. Each technology has its unique advantages, drawbacks, and challenges, with the field that continues to advance rapidly.
In this work, it has been decided to explore the domain of molecular qubits investigating the possibility of embedding an optical-active defect, the NV-center, inside small diamond nanoparticles. For this reason, it is necessary to understand all the characteristics that could make this system a reliable platform on which building a quantum computer that fulfills the DiVincenzo criteria.

1.2. Nitrogen Vacancy Center in Diamond

The nitrogen-vacancy (NV) center in diamonds has rapidly emerged as one of the most promising solid-state systems for quantum information processing and nanoscale quantum sensing. This optically active point defect consists of a substitutional nitrogen atom adjacent to a vacancy in the diamond crystal lattice (in figure 1.6).

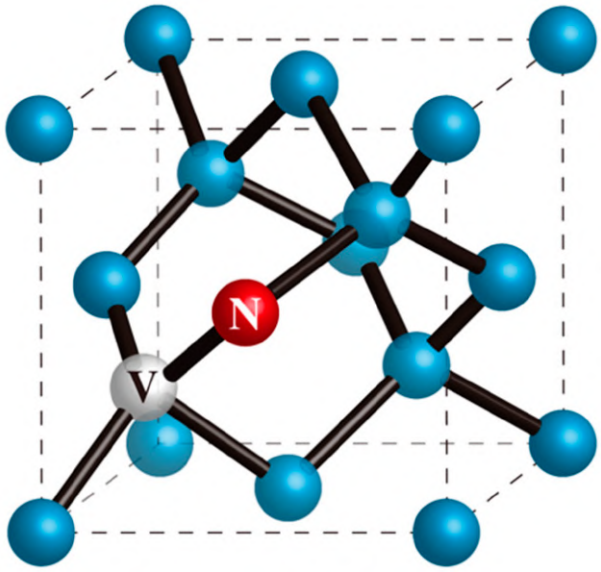

Figure 1.6: Atomic structure of the NV-center. [23]

In its negatively charged state (NV^-), it possesses a unique combination of spin and optical properties that make it remarkably suited for quantum technologies.
The development of strong theoretical approaches to model the defect's properties in harmony with first-principles calculations has been instrumental in supporting the growth of NV-center applications. These approaches have yielded crucial insights into the defect's optical properties, response to perturbations, electronic structure, and spin dynamics.
The promise of NV^- centers for quantum information stems from their optical addressability and spin coherence at room temperature.
The combination of long spin coherence and optical spin control has enabled demonstrations of quantum algorithms at room temperature using one or a few NV^- center qubits [46]. Key milestones include the entanglement of two proximal nuclear/electronic qubits, quantum teleportation across macroscopic distances, rudimentary quantum error correction algorithms, and basic quantum simulations using 2 qubit registers [51]. This defect occurs naturally in most diamond samples, though at low concentrations which are influenced by growth conditions and impurity levels (< 1 *ppm*) [44]. The negative

charge state NV^- can be produced via electron donation from nearby nitrogen donors or photo-excitation, so the NV^- has six electrons, five from nitrogen and one donated to the vacancy.
Ion implantation is a common technique to generate ensembles of NV^- centers, where vacancies are first created by irradiating the diamond sample with high-energy particles. Subsequent annealing leads to vacancy diffusion and some vacancies pair with existing nitrogen atoms to form NV centers. Shallow, individual NV^- centers, which are crucial for nanoscale sensing, are produced by implanting nitrogen at low energies ($5 - 10\ keV$) in high-quality, low-nitrogen diamond. Additional processing like surface oxidation is needed for charge state stabilization.
Recently, advances in chemical vapor deposition (CVD) growth have enabled direct, in situ formation of NV^- during synthesis. While challenges remain in controlling location, this offers a path to realizing large-scale quantum technologies using engineered NV^- defect arrays. Overall, the dream of practical quantum computing and sensing with NV centers critically depends on synthesis and fabrication advances guided by understanding gained from atomic-scale modeling. [54]

Electronic Structure

The ground state of the negatively charged NV center is a spin triplet with ${}^3A_2$ symmetry. This, in the single particle model, arises from six electrons in the a_1, e_x, and e_y orbitals localized on the three carbon dangling bonds and the nitrogen atom surrounding the vacancy. The degeneracy of the $m_s = \pm 1$ and $m_s = 0$ spin states is lifted by 2.87 GHz due to spin-spin dipolar interactions, giving this characteristic zero-field splitting, crucial for quantum information science applications. Hyperfine interactions with nearby nuclear spins can reach several MHz and are critical for entanglement schemes with the electron spin [54].

The lowest-energy optically excited state is also a spin triplet labeled ${}^3E$, predominantly involving an electron excitation from the a_1 to $e_{x,y}$ orbitals of the minority spin channel. The optical transition preserves spin and exhibits a broad phonon sideband, attributed to significant electron-phonon coupling effects.
Spin-orbit and spin-spin dipolar interactions give fine structure splittings on the order of gigahertz (5.33 GHz) in the ${}^3E$ state [54].
Quantitative prediction of the excited state properties requires going beyond the standard Born-Oppenheimer approximation and diagonalizing the full electron-phonon Hamilto-

nian. However, spin-orbit couplings are significantly underestimated compared to experiments. More accurate methods like configuration interaction (CI) are needed but require large supercells and are computationally demanding.

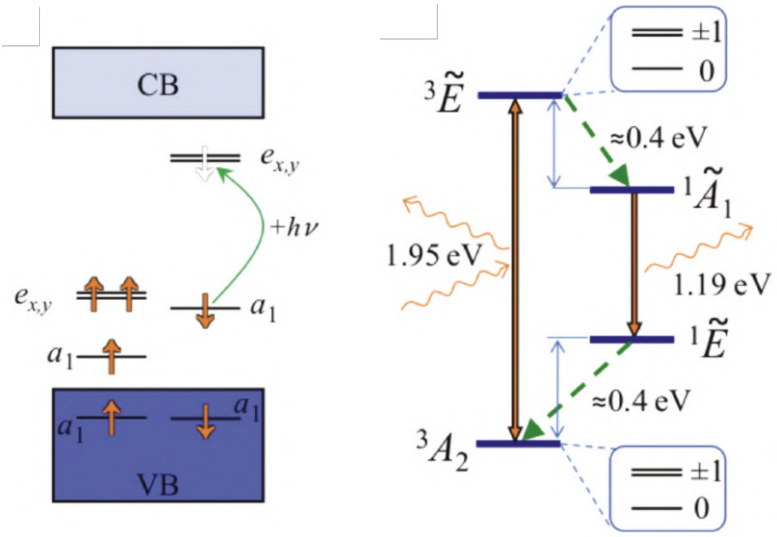

(a) Single particle NV-center electronic structure in the $^3A_2$ ground state.

(b) Many body NV-center electronic structure.

Figure 1.7: Electronic structure of the negatively charged NV-center. [54]

The primary competing decay process from the ^3E excited state is intersystem crossing to the $^1A_1$ singlet state, enabled by spin-orbit coupling. This crossing is spin-selective and gives rise to the possibility of adopting optical spin readout techniques. However, the singlet states are highly correlated and not well described by density functional theory calculation. Multireference methods have found the $^1A_1$ state to lie $\sim 0.4\ eV$ below the ^3E state and contains some $^1E'$ character.

The subsequent singlet decay back to $^3A_2$ is also spin-selective due to spin-orbit and phonon couplings in the ^1E state.

Strains, electric fields, and temperature shifts can tune the excited state fine structure on MHz to GHz scales. This enables control over the intersystem crossing rates and optical readout process. However, quantitative prediction remains challenging, with discrepancies up to an order of magnitude compared to experimental parameters. Further advances in excited state electronic structure methods are critical for design and optimization.

Optical Cycle for Spin Readout

A crucial property of the NV$^-$ center is that its electron spin state can be initialized and read out using visible light, even at room temperature. This capability relies on a complex interplay of radiative and non-radiative pathways linking the $^3A_2$, ^3E, and singlet states, as can be seen in figure 1.8.

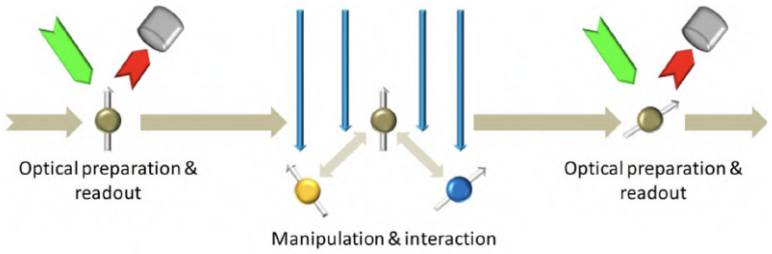

Figure 1.8: Scheme of the prepare, manipulate or interact, readout mode of operation of the NV$^-$ spin qubit [13].

After green (520 nm) excitation from $^3A_2$ to ^3E, the $m_s = \pm 1$ sublevels preferentially decay to the singlet states via spin-selective intersystem crossing (ISC). Spin-orbit coupling enables transitions between the ^3E triplet and singlet states. The ISC leads to around 50% higher fluorescence from the $m_s = \pm 1$ sublevels compared to $m_s = 0$ sublevel [13]. This optical spin contrast enables optical detection of spin resonance using optically detected magnetic resonance (ODMR).
DFT calculations of spin-orbit and electron-phonon coupling strengths have shed important light on this ISC process.

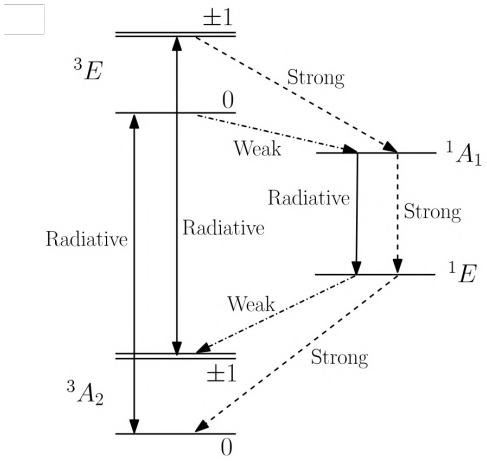

Figure 1.9: Many body NV$^-$ electronic structures with radiative and non-radiative transitions [13].

The spin-dependent intersystem crossing rates from ^3E to $^1A_1$ exhibit a nontrivial temperature dependence, so proper modeling requires vibronic solutions that combine the electronic and phonon coordinates.
One signature of efficient ISC is the large phonon sideband in the NV$^-$ optical spectrum since phonons assist triplet to singlet transitions.
While limitations exist in accurately modeled the strongly correlated singlet states, advanced DFT methods have clearly elucidated the key spin-dependent mechanisms enabling NV$^-$ optical spin readout.

Photoionization for Spin Readout

An alternative technique to read out the NV-spin state optically is photocurrent detection, which relies on spin-dependent photoionization from the defect. Here, green light excitation followed by a second photon absorption ionizes the NV$^-$ by ejecting an electron into the diamond conduction band. Since the ^3E lifetime depends on the spin state, this leads to spin-contrasted photocurrents [54].
Remarkably, DFT helped uncover that unlike most color centers, a critical role in efficiently ionizing NV$^-$ is played by an Auger recombination process. After photoexcitation into the conduction band, the high-energy electron relaxes back and uses the energy gain to ionize another electron rather than emitting a photon. This unusual Auger process dominates over the generally stronger single optical transition for ionization [54].

Sensing Application

The NV$^-$ center is also extremely useful as a nanoscale quantum sensor owing to the high sensitivity of its spin sublevels to external perturbations. The defect's atomic size, biological compatibility, and non-invasive optical readout make it ideal for nanometrology and bioimaging under ambient conditions. NV$^-$ magnetometry using a single qubit has achieved detecting fields down to 0.9 $\frac{pT}{\sqrt{Hz}}$ [8], enabling applications from record storage to neuronal current mapping. Likewise, the dipole moment change between ground and excited states allows all-optical NV$^-$ electrometry down to 1 $\frac{V}{cm\cdot\sqrt{Hz}}$ [10]. Local strain/stress fields shift the NV$^-$ ground state splitting, enabling also nanomechanical sensing. Rates of spin dephasing and intersystem crossing depend on temperature, allowing nanothermometry using NV$^-$. Much ongoing research focuses on improving the precision and spatial resolution of NV-based field sensors using advanced diamond nanofabrication, quantum control protocols, and signal processing algorithms. In parallel, first-principles theory has

delivered important insights about the defect's Hamiltonian parameters and noise properties to guide optimized quantum sensing. Quantifying spin susceptibility to perturbations like magnetic fields via ab initio techniques supports the design of new quantum sensing modalities with NV^- to broadly impact technology and science. [54]

1.3. Diamondoids: sp^3 Carbon Nanostructures

The other crucial component of the system that has been analyzed is the hosts of the NV-center.
Diamondoids are a class of nanometer-sized hydrocarbon molecules that have a structure resembling that of diamonds. They are composed of carbon and hydrogen atoms arranged in a three-dimensional, cage-like structure. The name "diamondoid" is derived from the fact that their structure is similar to that of a tiny diamond crystal.

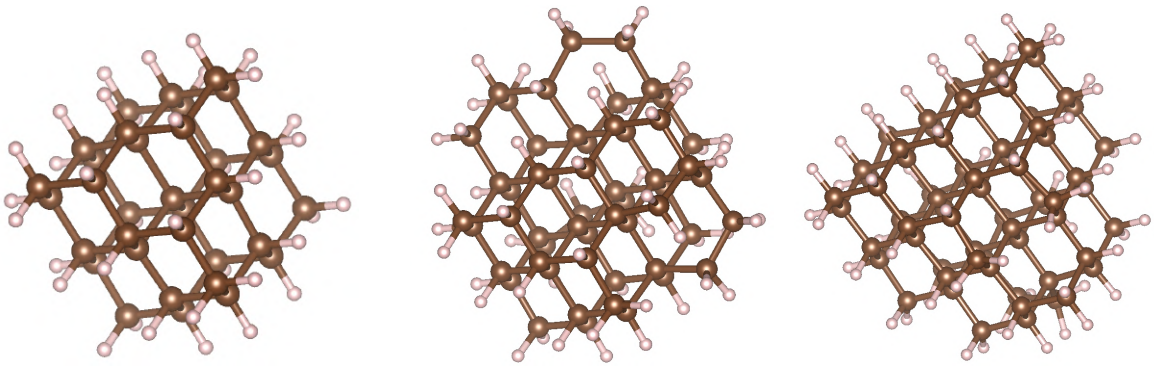

(a) $C_{35}H_{36}$ (b) $C_{54}H_{56}$ (c) $C_{69}H_{62}$

Figure 1.10: Different dimension diamondoids used in this work.

Diamondoids occur naturally in small quantities in petroleum deposits and certain types of minerals, but they can also be synthesized in the laboratory, ranging from adamantane ($C_{10}H_{16}$, ~ 3 Å carbon cage diameter) to larger nanodiamonds with intricately arranged carbon atoms (tens of nm diameter). Producing diamondoids involves intricate synthesis processes, often starting from readily available hydrocarbon precursors. One common approach is bottom-up synthesis, where smaller diamondoids are built up through controlled chemical reactions. The diamondoid growth process involves precise manipulation of reaction conditions, such as temperature and pressure, to ensure the correct bonding patterns [36, 41, 53].
They are of significant interest in various fields, including chemistry, materials science, and nanotechnology, due to their unique properties, such as extreme hardness and high

thermal stability, due to their covalent nature.
Diamondoids have been previously studied using first-principles calculations, providing insights into their atomic and electronic structures: methods like density functional theory (DFT) and quantum Monte Carlo (QMC) have been applied.
Calculations predict that diamondoids show quantum confinement effects below 1 nm in size, with HOMO-LUMO gaps larger than bulk diamond, and negative electronic affinity [15].

1.3.1. Incorporating NV-Centers into Diamondoids

The endeavor to integrate NV-centers into diamondoids originates from the desire to harness their advantageous properties for quantum computing. The NV-center, with its unique spin properties and coherence time behavior, presents an attractive avenue for constructing robust qubits, but encapsulating an NV-center within a diamondoid structure aims to leverage the molecular framework for enhanced tunability while preserving the NV-center's quantum properties.

Diamondoids, due to their discrete nature, provide a platform for isolating and manipulating individual qubits. This molecular confinement introduces a level of isolation that minimizes environmental interactions and could enhance qubit coherence. In addition, previous works have demonstrated the possibility of implanting and manipulating NV centers inside nanodiamonds paving the way to the foundation of this work [33].

1.4. Aim of the Thesis

Within this context, the aim of this thesis is to embark on an exploration into the realm of molecular qubit systems, with a specific focus on the potential of nitrogen-vacancy centers housed within nanodiamonds.
As said before, molecular qubits represent a promising frontier in quantum computing and quantum information science, so it is interesting to understand if it is possible to harness the robust properties of one of the most studied solid-state qubits, within a molecular environment. In fact, the NV-center embedded in diamond shows a long coherence time, which is crucial to store the information in a robust spin state, even at room temperature. For these reasons, it is completely worth to explore as many systems integrating this type

of molecular qubit as it is possible, also because the systems that will be analyzed in this work, have not been yet explored intensively with experiments and calculations, in particular with Density Functional Theory (DFT) plane waves calculations.
In first analysis, this thesis will be focused on the calculations of the isolated nanoparticles' electronic structure, to gain preliminary knowledge of the system and to understand whether the NV-center in a pristine diamondoid could be used to store quantum information.
Then, the nanoparticle surface will be functionalized, to engineer the electronic properties of the molecule favorably from the point of view of system stability.
Finally, it will be explored the possibility of integrating the qubits in a molecular crystal, to exploit the effect of pressure, which could be vital in stabilizing even more the NV-center, and the molecular environment, which allows longer coherence time, due to the less interference with respect to the solid-state case.
In essence, this thesis aims to illuminate the unexplored territories of molecular qubits and their potential integration into real hardware, utilizing plane waves DFT calculations serving as a working tool.

2 | Theoretical Framework: the Density Functional Theory (DFT)

This section delves into the foundational principles and core concepts underpinning Density Functional Theory (DFT).
DFT is the powerful computational framework employed in this work and within the quantum chemistry and condensed matter physics communities, DFT stands as an indispensable tool, offering a robust theoretical foundation for elucidating a wide spectrum of phenomena, ranging from intricate molecular interactions to the behavior of solid materials.
In this work, the DFT is used within a framework that uses a fundamental approximation: the Born-Oppenheimer approximation.

2.1. Born-Oppenheimer Approximation

The Born-Oppenheimer approximation is a fundamental concept in quantum chemistry and condensed-matter physics since it simplifies the quantum mechanical description of the analyzed system by separating the motion of electrons and nuclei.

The nuclei, which are much heavier than electrons, move more slowly, so it is possible to assume that the electronic and nuclear motions are decoupled. This approximation allows to write the following Schrödinger equation:

$$H_{\text{total}}\Psi(\mathbf{R},\mathbf{r}) = E\Psi(\mathbf{R},\mathbf{r}) \tag{2.1}$$

Here, $\mathbf{R}$ represents the nuclear coordinates, $\mathbf{r}$ represents the electronic coordinates, H_{total} is the system Hamiltonian, $\Psi(\mathbf{R}, \mathbf{r})$ is the system wave function, and E is the total energy.

The total Hamiltonian can be expressed as the sum of nuclear and electronic Hamiltonians:

$$H_{\text{total}} = H_{\text{nuclear}}(\mathbf{R}) + H_{\text{electronic}}(\mathbf{r}|\mathbf{R}) \tag{2.2}$$

$H_{\text{electronic}}$ represents the electronic Hamiltonian expressed as a function of electronic coordinates, $\mathbf{r}$, parametrically dependent on nuclear coordinates, $\mathbf{R}$.

In this context, it is possible to exploit ground-state DFT calculation, treating the nuclear positions as if they were fixed.
Clearly, more advanced methods, built on top of single-point DFT calculations, are needed to include the vibrational properties of the system inside the electronic structure.

2.2. Foundations of DFT

Among all the quantum mechanics principles, Density Functional Theory (DFT) is based on the fundamental concept of electron density, the Hohenberg-Kohn theorems, and the auxiliary system of equations proposed by W. Kohn and L.J. Sham.

2.2.1. Electron Density and Hohenberg-Kohn Theorems

The central quantity of interest is the electron density, denoted as $\rho(\mathbf{r})$, where $\mathbf{r}$ represents the spatial coordinates. The electron density describes the probability of finding an electron at a particular point in space, and it is defined as:

$$\rho(\mathbf{r}) = \sum_{i=1}^{N} |\Psi_i(\mathbf{r})|^2, \tag{2.3}$$

where $\Psi_i(\mathbf{r})$ is the wave function of the i-th electron, and N is the total number of electrons.

P. Hohenberg and W.Kohn proposed the other cornerstone of DFT with their theorems

that can be summarized as follows:

1. **First Hohenberg-Kohn Theorem:** The external potential $V(\mathbf{r})$ that minimizes the electronic ground-state energy uniquely determines the ground-state electron density $\rho(\mathbf{r})$. In other words, there is a one-to-one correspondence between the external potential and the electron density.

2. **Second Hohenberg-Kohn Theorem:** There exists a universal functional, $F[\rho]$, of the electron density, such that the ground-state energy E_0 is minimized when the true electron density $\rho(\mathbf{r})$ is used:

$$E_0 = \min_{\rho(\mathbf{r})} \left[T[\rho] + U[\rho] + \int V(\mathbf{r})\rho(\mathbf{r})\, d\mathbf{r} + E_{\text{xc}}[\rho] \right], \tag{2.4}$$

$$U[\rho] = \frac{1}{2} \int \frac{\rho(\mathbf{r})\rho(\mathbf{r}')}{|\mathbf{r} - \mathbf{r}'|}\, d^3\mathbf{r}\, d^3\mathbf{r}', \tag{2.5}$$

   where $T[\rho]$ is the kinetic energy, $V(\mathbf{r})$ is the external potential, $U[\rho]$ is the electron-electron repulsion energy in the Hartree approach, and $E_{\text{xc}}[\rho]$ is the exchange-correlation energy, which incorporates the effects of electron-electron correlation beyond the mean-field approximation. These effects are crucial to accurately predict the properties of the system.

2.2.2. Kohn-Sham Equations

Along with the functional expression of the ground-state energy, to make DFT computationally tractable, Kohn and Sham introduced a set of fictitious non-interacting electrons that have the same ground-state electron density as the real interacting electrons. The Kohn-Sham equations are a set of equations for these fictitious electrons:

$$\left[-\frac{1}{2}\nabla^2 + V_{\text{eff}}(\mathbf{r}) \right] \phi_i(\mathbf{r}) = \epsilon_i \phi_i(\mathbf{r}), \tag{2.6}$$

where $\phi_i(\mathbf{r})$ are the Kohn-Sham orbitals, ϵ_i are their corresponding eigenvalues, and $V_{\text{eff}}(\mathbf{r})$ is the effective potential:

$$V_{\text{eff}}(\mathbf{r}) = V(\mathbf{r}) + V_{\text{H}}(\mathbf{r}) + V_{\text{xc}}(\mathbf{r}), \tag{2.7}$$

with $V(\mathbf{r})$ being the external potential, $V_{\text{H}}(\mathbf{r})$ the Hartree potential arising from electron-electron repulsion, and $V_{\text{xc}}(\mathbf{r})$ the exchange-correlation potential.

2.2.3. Exchange Correlation Functionals in DFT

As was said before, correlation is extremely important in DFT calculation and it refers to the electron-electron interactions that are not accounted for in the mean-field approximation. This includes both electron-electron correlation effects and exchange interactions. The exchange-correlation energy, $E_{\text{xc}}[\rho]$, in the second Hohenberg-Kohn theorem captures these effects and is typically approximated using various functionals, which have been developed over the years, each with its own strengths and weaknesses.

Local Density Approximation (LDA)

The Local Density Approximation (LDA) is the simplest category of exchange-correlation functionals. [29] It assumes that the exchange-correlation energy at a given point in space depends only on the electron density $\rho(\mathbf{r})$ at that point. The LDA exchange-correlation energy is given by:

$$E_{\text{XC}}^{\text{LDA}}[\rho] = \int \rho(\mathbf{r})\epsilon_{\text{XC}}^{\text{hom}}(\rho)\, d\mathbf{r}, \tag{2.8}$$

where $\epsilon_{\text{XC}}^{\text{hom}}(\rho)$ is the exchange-correlation energy per electron of a uniform electron gas with density ρ.

LDA functional is computationally efficient and gives reasonable results for systems such as the Homogeneous Electron Gas (HEG) and the H_2 molecule, but it overestimates the binding energies and it in general fails in systems in which correlation contribution is important with respect to the exchange, since it does not predict accurately the correlation effects [38].

Perdew-Burke-Ernzerhof (PBE) Functional

The Perdew-Burke-Ernzerhof (PBE) [42] functional is a widely used generalized gradient approximation (GGA) exchange-correlation functional, and it has been used in this work for all the performed calculations. Unlike LDA, it takes into account the gradient of the electron density, making it more accurate for a broader range of systems. The PBE exchange-correlation energy can be written as:

$$E_{\text{XC}}^{\text{PBE}}[\rho] = \int \rho(\mathbf{r})\epsilon_{\text{XC}}^{\text{PBE}}(\rho, \nabla\rho)\, d\mathbf{r}, \tag{2.9}$$

where $\epsilon_{XC}^{PBE}(\rho, \nabla\rho)$ is a functional that depends on both the density and its gradient.

PBE is known for its balanced accuracy and efficiency and is often also used as a baseline functional for a wide range of DFT calculations.

Strongly Constrained and Appropriately Normed (SCAN) Functional

Another functional that is encountered in this thesis is the SCAN (Strongly Constrained and Appropriately Normed) functional [49]. It is a recent development in DFT, and it falls within the broader category of meta-GGA (meta-Generalized Gradient Approximation) functionals.
These functionals have gained significant attention in the field of computational chemistry due to their ability to provide accurate and reliable predictions of various molecular properties. They are built on the GGA approach by considering additional gradients of the electron density, so they are more complex than GGA functionals but offer improved accuracy for a wide range of systems.
The SCAN functional performs exceptionally well in predicting molecular geometries, cohesive energies, and chemical reactions. Moreover, it has also been valuable in describing challenging systems in which van der Waals interactions and hydrogen bonds play a major role [48].

Hybrid Functionals

An important class of functional, that has to be cited even if it has not been exploited in this work, is the hybrid functional class.
These functionals are built as a linear combination of the Hartree-Fock exchange energy and any number of exchange and correlation explicit density functionals.
Hybrid functionals are known to provide better accuracy for certain types of systems, such as those involving transition metals or molecules with strongly correlated electrons. Among the various hybrid functionals that have been developed, it is worth citing the B3LYP functional [7], PBE0 functional [3], and the HSE functional [21].
The choice of exchange functional in DFT calculations depends on the specific system being studied and the desired level of accuracy. While GGAs like PBE are often suitable for many materials, hybrid functionals like B3LYP and HSE provide enhanced accuracy for systems in which the exchange contributes to the total energy is particularly relevant. In practice, it is common to benchmark different exchange functionals against experimen-

tal data or higher-level quantum chemical methods to determine which functional best describes the properties of interest.
In this work, the hybrid functionals were not used due to their high computational time. For the opposite reason, the LDA functional is not used as well. Its simplicity does not allow to obtain an accurate electronic structure that can capture the main features of the NV-center in nanodiamonds.
In this context, the PBE functional seemed to be the best choice to explore a vast amount of structures, obtaining insightful results to be compared with reference calculations of similar structures investigated using the same functional.

2.3. Basis Sets in DFT

Another role of major importance in the practical implementation of Density Functional Theory (DFT) is played by basis sets. They provide a systematic way to represent the electronic wavefunctions and the density of the system that has to be analyzed.
In this section, some common types of basis sets used in DFT calculations will be explored to understand the advantages and drawbacks of each of them.

2.3.1. Plane Wave Basis Set

The plane wave basis set represents the electronic wavefunctions using a set of plane waves with wave vectors ($\mathbf{k}$), in fact, the electronic wavefunctions $\psi(\mathbf{r})$ are expanded as follows:

$$\psi(\mathbf{r}) = \sum_{\mathbf{k}} c_{\mathbf{k}} e^{i\mathbf{k}\cdot\mathbf{r}}$$

where $c_{\mathbf{k}}$ are expansion coefficients.
Plane waves provide a complete basis set that satisfies the periodic boundary conditions of crystals so they can accurately describe the electronic structure of periodic systems.
The use of this basis set is not limited just to periodic systems but is also exploited in molecules and more localized systems calculation since force evaluation is particularly accurate.
However, it is not efficient when it deals with localized systems, since large cells are needed to avoid spurious periodic-images interactions. In fact, the main drawback that sometimes makes the plane waves choice unfavorable is the computational resources needed.

2.3.2. Gaussian Basis Set

When it is necessary to deal with localized systems, one of the best choices is relying on the Gaussian basis set. This method can be understood as a hybrid between a tight binding approach and the DFT plane waves approach. The electronic wavefunctions are expanded in terms of Gaussian basis functions centered on atomic nuclei:

$$\psi(\mathbf{r}) = \sum_i c_i \exp\left(-\frac{(\mathbf{r}-\mathbf{R}_i)^2}{2\sigma_i^2}\right)$$

where c_i are coefficients, σ_i controls the width of the gaussians, and $\mathbf{R}_i$ are atomic positions.

This method doesn't imply the use of strict atomic orbitals, in fact, the Gaussian functions are highly flexible and can be tailored to describe a wide range of chemical systems. However, as in the case of plane waves, the Gaussian basis set may require a large number of functions to accurately describe extended systems, and its implicit localization makes it unfavorable to use in highly delocalized systems.
Moreover, this basis set does not allow to establish the periodic boundary conditions straightforwardly and to evaluate accurately the forces.

2.3.3. Augmented Plane Wave Basis Set

Another interesting approach is the Augmented Plane Waves (APW) basis set, which combines aspects of plane waves and localized basis functions. In APW, the wavefunctions are expressed as a linear combination of plane waves and atomic-like functions within muffin-tin spheres:

$$\psi(\mathbf{r}) = \sum_{\mathbf{k}} c_{\mathbf{k}} e^{i\mathbf{k}\cdot\mathbf{r}} + \sum_{\text{atoms}} \sum_{lm} c_{lm} \frac{f_l(r)}{r} Y_{lm}(\theta,\phi)$$

where $f_l(r)$ are radial functions, $Y_{lm}(\theta,\phi)$ are spherical harmonics, and $c_{\mathbf{k}}$ and c_{lm} are coefficients.

APW combines the accuracy of plane waves for extended systems with the locality of atomic-like functions. For this reason, it provides a balanced description of core and va-

lence electrons. However, APW calculations can be computationally demanding due to the need for multiple basis functions, and the choice of parameters, such as the number of plane waves and the size of muffin-tin spheres, can affect accuracy.

2.3.4. Pseudopotentials in DFT Calculation

It's important to note that the choice of basis set and its parameters (e.g., cutoff energies for plane waves) can significantly affect the accuracy of DFT calculations, so basis set optimization can be performed to strike a balance between computational cost and precision.
Pseudopotentials are an essential tool in Density Functional Theory (DFT) that simplify electronic structure calculations by effectively removing the core electrons from the problem, allowing for more computationally efficient and accurate calculations.

The core electrons are relatively unreactive and do not significantly contribute to the bonding and chemical behavior of atoms or molecules. Their inclusion in calculations is computationally expensive and can lead to convergence difficulties, especially when dealing with transition metals and heavy elements.

Pseudopotentials are introduced to replace the effect of core electrons with an effective potential that reproduces their influence on the valence electrons accurately.

However, it is important to be aware of the limitations of pseudopotentials:

- Choice of pseudopotential can affect the accuracy of results, so careful selection is crucial.
- Pseudopotentials optimized for one type of calculation may not be suitable for another.
- Limited applicability in certain situations, such as when studying core-level spectroscopy or very high-precision calculations.

In particular, if a pseudopotential is used in combination with plane waves, it is possible to exploit the accuracy of this basis set to predict the most important behavior of electrons in the system, without the huge computational time required if the core electrons are considered during the algorithm iterations, since these electrons are also the most

localized and, for this reason, the most difficult to represent in the plane waves basis set.

At this point, it should be clear the importance of the choice of the basis set in DFT calculations, which depends on the nature of the system being studied and the trade-off between accuracy and computational efficiency.
In this work, it has been used the combined approach of plane waves for the valence electronic wavefunctions and pseudopotentials to describe the core electrons. This hybrid approach allows for accurate and efficient calculations of complex materials, even if in the first stage of the project it was needed to deal with molecular systems.
It is important to underline that the secondary aim of this thesis is to obtain accurate insight into the system, using this completely novel approach in the context of NV-center embedded in nanodiamonds.
However, the substantial advantage of using plane waves has been exploited with the molecular crystal's calculations since the convergence in these periodic systems is much faster.

2.4. Electron-Phonon Interaction

As was previously mentioned in this chapter, the Born-Oppenheimer approximation prevents the electron-phonon interaction from being included in a single-point DFT calculation; however, several types of statistical algorithms can be established to retrieve the phonon effect using DFT single-point calculations.
This avoids the need for computationally costly quantum molecular dynamics simulations while still enabling the computation of the electron-phonon renormalization with a certain level of statistical accuracy.

2.4.1. Molecular Dynamics Formulation and Electron-Phonon Coupling

The Born-Oppenheimer approximation states that the Hamiltonian of a system composed of electrons and nuclei can be described by the equation 2.2, and the nuclear Hamiltonian is:

$$\hat{H}_{nuc} = -\frac{\hbar^2}{2}\sum_{I=1}^{N_{nuc}}\frac{1}{M_I}\nabla_I^2 + V(\mathbf{R}) \tag{2.10}$$

where M_I is the mass of nucleus I. $V(\mathbf{R})$ represents the 3N-dimensional adiabatic potential energy surface, that couples the nuclear and electronic degrees of freedom.
Solving the nuclear Schrödinger equation yields quantized vibrational modes called phonons. Every electronic property at a given generic temperature T can be calculated as the ensemble average over all the adiabatic nuclear states, taking into account the influence of electrons and phonons. [30][31]

$$\langle\mathcal{O}\rangle_T = \frac{1}{Q(T)}\sum_{k=0}^{\infty}\left\langle\chi_k(\mathbf{R})|\hat{\mathcal{O}}(\mathbf{R})|\chi_k(\mathbf{R})\right\rangle\exp\left(-\frac{\varepsilon_k}{k_BT}\right) = \int d\mathbf{R}W(\mathbf{R},T)\mathcal{O}(R) \tag{2.11}$$

where $|\chi_k(\mathbf{R})\rangle$ is one of the eigenstates of the nuclear Hamiltonian and $Q(T)$ is the partition function.
In a quantum molecular dynamics simulation, the vibrational states of the systems can be evaluated following a quantum thermostat approach or the path integral formulation, and the thermal average of the electronic property analyzed is retrieved from the equation 2.11.
Due to the high computational cost of these calculations, the harmonic approximation is a popular method for recovering the electron-phonon renormalization. [30][31]

2.4.2. Harmonic Approximation

The harmonic approximation assumes that the potential energy surface $V(\mathbf{R})$ near equilibrium is quadratic:

$$V^H(\mathbf{R}) = \frac{1}{2}\sum_{I\alpha,J\alpha'}\left(R_{I\alpha}\sqrt{M_I}\right)D_{I\alpha,J\alpha'}\left(\sqrt{M_J}R_{J\alpha'}\right) \tag{2.12}$$

$$D_{I\alpha,J\alpha'} = \frac{1}{\sqrt{M_IM_J}}\frac{\partial^2\mathcal{V}(\mathbf{R})}{\partial R_{I\alpha}\partial R_{J\alpha'}}\bigg|_{\mathbf{R}=\mathbf{0}} \tag{2.13}$$

The normal modes are decoupled simple harmonic oscillators. This enables the analytical solving of the nuclear problem to obtain [30]:

$$\langle \mathcal{O} \rangle_T^{\mathrm{H}} = \int d\mathbf{X} W^{\mathrm{H}}(\mathbf{X}, T) \mathcal{O}(\mathbf{X}) = \int d\mathbf{X} \left[\prod_{\nu=3+d_r+1}^{3N} G\left(X_\nu; \sigma_{\nu,T}\right) \right] \mathcal{O}(\mathbf{X}) \tag{2.14}$$

$$\sigma_{\nu,T} = \sqrt{\frac{2n_B\left(\omega_\nu, T\right) + 1}{2\omega_\nu}}. \tag{2.15}$$

$$n_B(\omega, T) = \frac{1}{\exp\left(\omega / k_B T\right) - 1} \tag{2.16}$$

Clearly, the harmonic approximation neglects the anharmonicity effect of the potential energy surface, and strong electron-phonon coupling and phonon-phonon scattering effects can lead to significant deviations.

2.4.3. Statistical Approaches for Electronic Quantities

The key idea of statistical approaches is to sample the quantum nuclear distribution $W^H(\mathbf{R}, T)$ to compute the thermally averaged electronic properties.
In a Monte Carlo approach at each step, a set $\mathbf{X}^i$ of displaced normal mode coordinates is gathered.
Then, the normal mode displacements are transformed to Cartesian displacements and the electronic property is computed in that nuclei configuration. [30][31]
In this way the thermal averaged electronic property is calculated as follows:

$$\langle O \rangle_T \approx \frac{1}{M} \sum_{i=1}^{M} O(\mathbf{R}^i) \tag{2.17}$$

where M is the sample size and $\mathbf{R}^i$ are the displaced Cartesian coordinates.
To extract the set of displaced normal modes it is possible to follow different approaches. One possible approach is to consider $\mathbf{X}^i = \mathbf{s}^i \boldsymbol{\sigma}_T$, where $\boldsymbol{\sigma}_T$ is the matrix that contains the broadening for each mode and $\mathbf{s}^i$ is a matrix with the first $3 + dr$ (dr depends on the system that has to be analyzed) elements set to zero, because they refer to the movement of the system as whole, and the remaining elements are either +1 or -1.
The signs of the displacement can be chosen according to different algorithms such as a Monte Carlo algorithm or a one-shot method. [30][31]
Moreover, an additional first-principles calculation on the antithetic pair of the chosen atomic configuration can improve the result.

3 | Materials and Methods

3.1. DFT Algorithm

In this section, the key steps of the DFT algorithm will be discussed, in order to understand the importance of parameter choice to obtain efficient and accurate calculations.

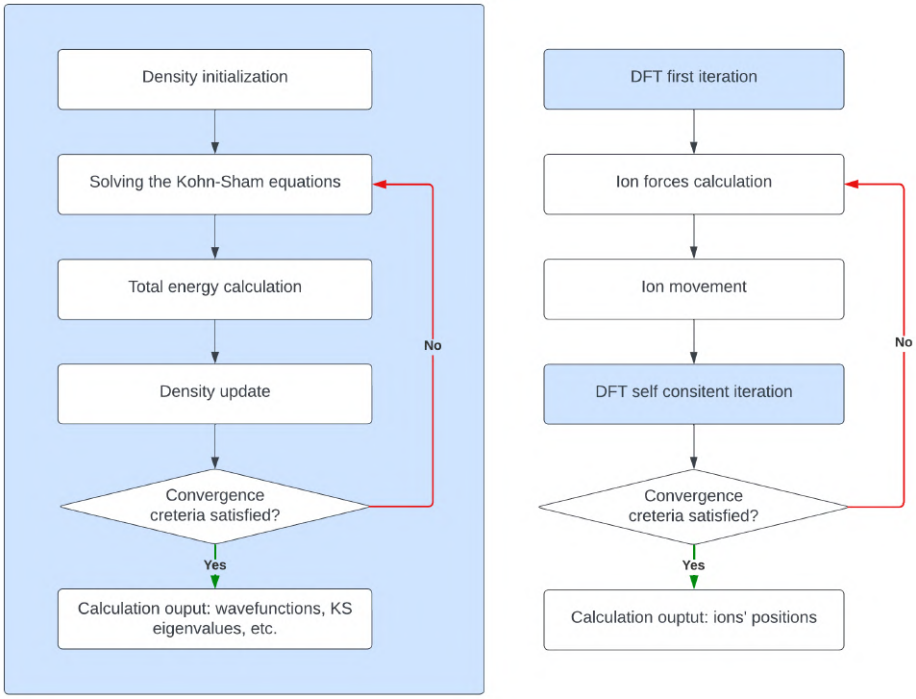

Figure 3.1: DFT algorithms representation for ground state calculations (left) and structure relaxation (right).

The DFT calculation begins with an initial guess for the electron density, $\rho^{(0)}(\mathbf{r})$, evaluated starting from the initial electronic wavefunctions $\Psi_i^{(0)}(\mathbf{r})$. It is important to note that when the symmetry of the atomic coordinate is high, the iterative algorithms may not lead to the right ground state. For this reason, slight symmetry breaking is used

by introducing random fluctuations in the wave functions, which is sufficient to ensure convergence to the right ground state.

The central step in the DFT algorithm is the solution of the Kohn-Sham equations, which are the set of single-particle Schrödinger-like equations for the Kohn-Sham orbitals $\phi_i(\mathbf{r})$ and their corresponding eigenvalues ϵ_i:

$$\left[-\frac{1}{2}\nabla^2 + V_{\text{eff}}^{(n)}(\mathbf{r})\right]\phi_i(\mathbf{r}) = \epsilon_i\phi_i(\mathbf{r}), \tag{3.1}$$

where $V_{\text{eff}}^{(n)}(\mathbf{r})$ is the effective potential at the n-th iteration, including the external potential, the Hartree potential, and the exchange-correlation potential. The Kohn-Sham orbitals and eigenvalues are updated at each iteration until self-consistency is achieved. The effective potential depends on the electron density, which evolves as the Kohn-Sham orbitals are updated.

Once the Kohn-Sham orbitals are determined, the total energy of the system is calculated. The total energy is the sum of several components:

$$E_{\text{total}}^{(n)} = T^{(n)} + U^{(n)} + V_{\text{ext}} + E_{\text{xc}}^{(n)} + E_{\text{nuclear}}, \tag{3.2}$$

$T^{(n)}$ is the kinetic energy of the electrons. $U^{(n)}$ is the electron-electron interaction energy, including the Hartree energy. V_{ext} is the external potential energy, typically arising from atomic nuclei. $E_{\text{xc}}^{(n)}$ is the exchange-correlation energy, the key component describing electron-electron correlations. E_{nuclear} is the nuclear repulsion energy.

After calculating the total energy the electron density $\rho^{(n+1)}(\mathbf{r})$ is updated. The loop continues until the electron density converges to a self-consistent solution, where $\rho^{(n+1)}(\mathbf{r})$ and $\rho^{(n)}(\mathbf{r})$ are nearly identical.

To determine when convergence is achieved, a convergence criterion is established, typically based on the change in the electron density or total energy between iterations. Common convergence criteria include a specified threshold for the change in electron density or total energy.

It is worth noticing that when it is needed to deal with structure relaxation, it is important to focus on the maximum force between the ions as the convergence criteria. In fact, the whole procedure is demonstrated in figure 3.1 where it is evident that between the ionic movement step are nested classic ground state self-consistent iterations.

3.2. Computational Details

In this section, the computational details and the critical choices made regarding simulation parameters required to accurately characterize the electronic properties of the system will be discussed. All calculations in this work were performed using Qbox [19], an open-source code dedicated to electronic structure simulations. This choice was motivated by the desire to leverage the advantages of plane waves in conducting calculations on molecular crystals composed of nanoparticles.

3.2.1. Computational Architectures and Benchmarking Phase

All the major computations shown in this work were carried out through the use of the Midway2 cluster provided by the University of Chicago RCC (Research Computing Center).
This cluster allows to perform both CPUs and GPUs calculations, although the codes that have been run during the development of this project are CPUs codes.

A preliminary step, before delving into the proper simulation of the systems analyzed, was the benchmarking phase.
It was crucial since a wrong resource allocation would have meant an unfeasible amount of computational hours or a computational power waste.
For this reason, it has been decided to perform a ground state DFT calculation on one of the structures used in this work, $C_{69}H_{62}$, in cells with dimensions ranging from 20 $Bohr$ to 100 $Bohr$, with increasing number of CPUs.
Figure 3.2 briefly summarizes the most important results of the benchmarking phase, which make clear the amount of time needed for each simulation (each node has a 184 Gb usable memory and is composed of 40 cores).

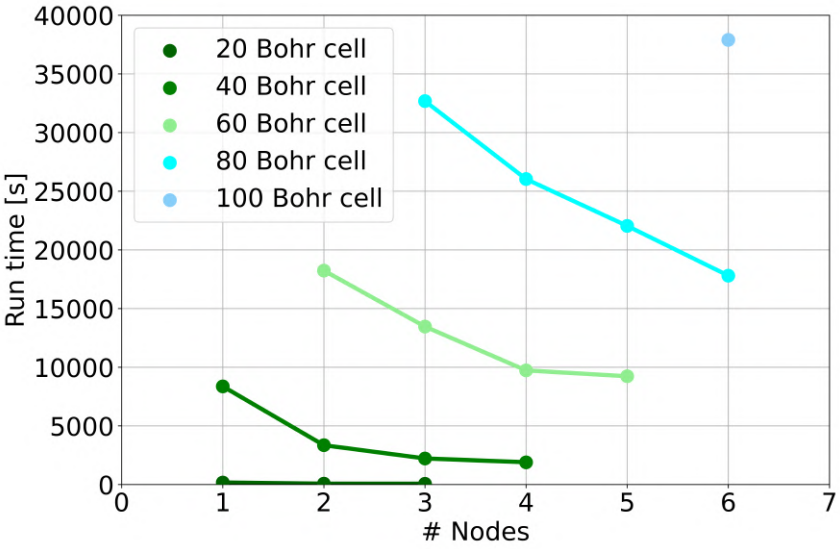

Figure 3.2: Run time analysis increasing the number of CPUs used.

3.2.2. Parameter Selection

To ensure reliable results, careful consideration was given to the selection of simulation parameters. These parameters play a pivotal role in the accuracy and efficiency of electronic structure calculations.

- **Energy Cutoff:** The energy cutoff determines the range of included plane waves in the calculation and was selected to balance accuracy and computational efficiency. Initially, we used an energy cutoff of 85.0 Ry as a reference. Later, we reduced it to 65.0 Ry to speed up calculations, since we obtained identical results with the latter cut-off.
- **Convergence Criteria:** Parameters related to self-consistency iterations and total energy convergence were finely tuned to ensure reliable results. We applied a tolerance of 10^{-8} eV for ground state calculations and 10^{-3} $Ha/Bohr$ for optimization calculations. For the most critical structure, optimization was further enhanced with a 10^{-4} $Ha/Bohr$ tolerance. On the other side, single optimization cycles with 10^{-2} $Ha/Bohr$ tolerance were carried out for systems needed to explore roughly some general electronic structure behaviors.
- **Cell Size:** As we are using periodic boundary condition (PBC) calculations, determining the cell size is crucial to minimize interactions between periodic images and accurately represent the system. In this study, the order of magnitude of the

Markov-Payne correction [37] was used as a reference to assess the difference between the nanodiamond's vacuum levels before and after NV implantation. It quickly became evident, given the flat potential at the cell boundaries, that a cell parameter of 40 *Bohr* was sufficient to avoid inter-cell interactions for neutral systems, and it is enough to converge at the right value for the HOMO-LUMO gap of the diamondoid, as it can be seen in figure 3.3. However, for charged systems, it was necessary to increase the cell parameter to 60 *Bohr*, resulting in a significant computational slowdown for these systems.

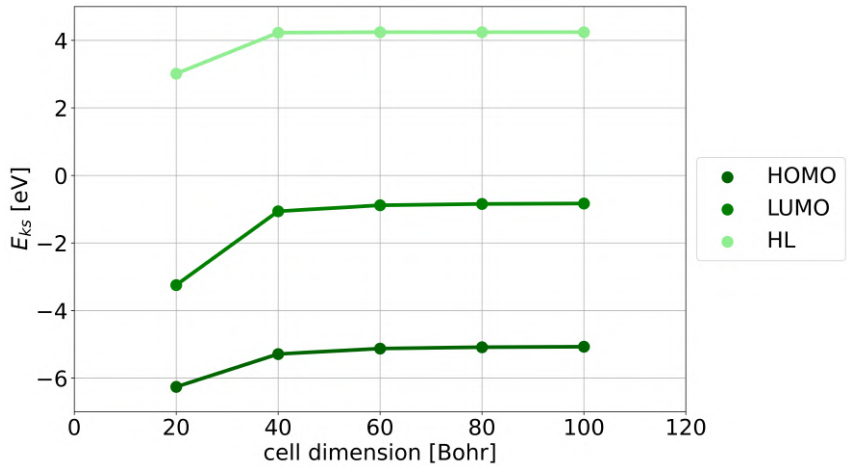

Figure 3.3: HOMO, LUMO, and HOMO-LUMO gap increasing the cell parameter for the $C_{69}C_{62}$ cluster.

- **Smearing Technique:** Smearing methods, which are used to treat electronic occupancies at finite temperatures, could be useful to speed up the calculations, so, we tried to use the Fermi smearing technique with the temperature fixed at 500 K. The main drawback is that for insulating systems, the smearing can give unreliable and un-physical results: it has caused a mixing of the levels that has reduced drastically the dimension of the gap. For this reason, no smearing technique was used in any of the calculations.

- **Optimization Algorithm:** The selection of an appropriate optimization algorithm can have different effects. First of all, it can impact the reliability of the results, so it has to be chosen properly. Then, obviously, it could help to speed up the calculations.
  In this work, the PSDA (Preconditioned Steepest Descent with Anderson acceleration) [4] algorithm and the JD (Jacobi-Davidson) [22] algorithm have been used together to combine quickness and reliability, since the PSDA algorithm alone is much

faster, but, when calculations with empty states are performed, it doesn't reach the accuracy of the JD algorithm. For this reason, a first PSDA self-consistence cycle has always been performed, followed by a JD cycle, whose starting point was the set of wavefunctions obtained during the PSDA iterations.

Lastly, a spin-polarized DFT calculation is needed when a system contains unpaired electrons because standard DFT calculations assume that electrons are spin-paired. For this reason, it was necessary to perform spin-polarized DFT calculation in the case of all the NV-nanodiamonds, starting from the assumption of having a triplet ground state.

3.2.3. Localization Approach

In this work, we are looking for localized single-particle defect levels near the vacancy, so it is necessary to define some measurement for this figure of merit.
We explored two different approaches: one is based on the inverse participation ratio (IPR) while the other is based on a selective integral of the wavefunction squared.
The IPR is a measure of the localization of a wavefunction [32] that is defined as:

$$IPR_i = \int |\Psi_i(\mathbf{r})|^4 dV, \tag{3.3}$$

Previously IPR has been used to characterize localized defect levels within disordered materials, for example, amorphous carbon [32]. The first approach relies on the comparison between the most localized orbital in the pristine nanostructure and each orbital in the NV-nanostructure: if the IPR of the wavefunction of the NV-nanostructure is higher than double the IPR of the pristine's most localized wavefunction, the NV one's is considered localized.

The second approach is local and relies on the calculation of the integral over the sphere or radius 1.5Å (C-C bond length) centered in the vacancy: if the orbital is more than 50% localized inside the sphere, it is considered localized.

$$loc_i = \int_{V \subseteq V_{sphere}} |\Psi_i(\mathbf{r})|^2 dV, \tag{3.4}$$

A similar approach has been used in previous works, to determine the localization of the NV-center orbitals. [45]

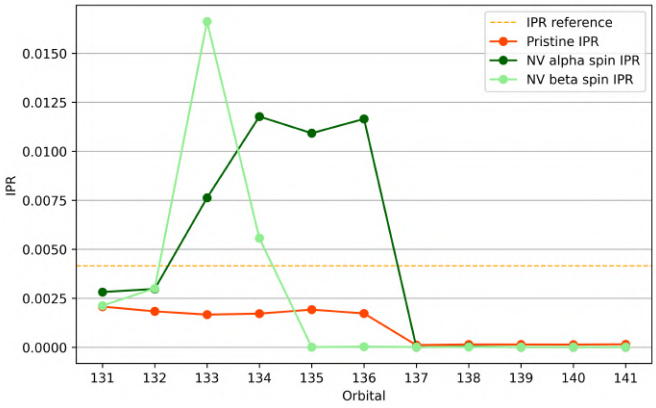

Figure 3.4: IPR analysis on the $C_{54}H_{56}$ cluster and its NV-embedded counterpart.

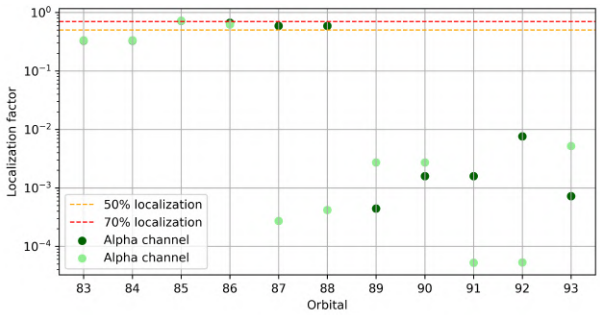

(a) $C_{33}H_{36}NV^-$ localization analysis.

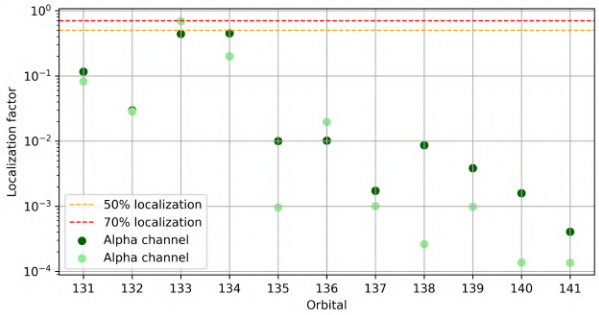

(b) $C_{52}H_{54}NV^-$ localization analysis.

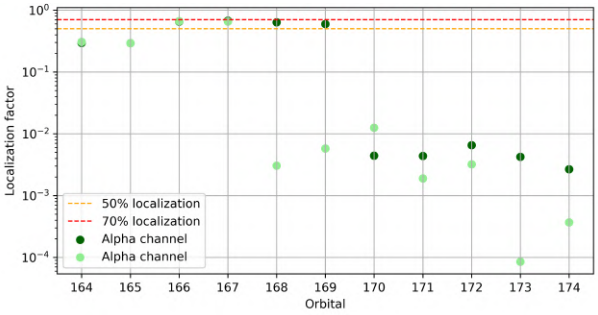

(c) $C_{67}H_{62}NV^-$ localization analysis.

Figure 3.5: Localization analysis results based on the local approach.

The reason why both of these methods were considered is that is difficult to define a measure for the localization in a molecular system, that is itself localized.
However, except where it is clearly mentioned, in this work the second method was chosen as the reference one since it allows to discriminate the position of the localization, so it is possible to understand where the orbital is localized, not just if it is localized.

4 | Electronic Structure of NV-nanodiamonds

In this chapter, we explore the selection of the nanoparticles to be analyzed, considering both their size and morphology. Additionally, we outline the methodology employed for the design and subsequently present the result of the analysis of the nanoparticles' electronic structure.

4.1. Structure Design

The nanoparticles under investigation in this study are small-size nanodiamonds.
There are several reasons for choosing such small structures, even if it has been demonstrated also the feasibility of bigger nanodiamonds production [53]:

1. **Computational Cost:** Computational resources are a critical aspect of this research. Smaller nanoparticles result in lower computational costs, that enable to explore a wider range of designs and configurations.

2. **Surface Effect in NV Diamond:** The NV-center in small-sized nanoparticles is affected by the surface effect that characterizes the NV-center when is embedded in diamond [54]. Although the proximity to the surface should be avoided, due to the negative electronic affinity (EA), it can be exploited by functionalizing the termination of the nanoparticles to improve the stability of the NV-center.

3. **Symmetric Behaviour:** The nanoparticles were designed to be not symmetrical. In this way, it would be possible to underline the effects of the broken symmetry on the electronic structures, which is an important point, since it is difficult in principle to control the symmetry of the nanoparticle during the synthesis. Moreover, non-symmetrical effects can be easily produced in small-sized nanoparticles.

4. **Qubits Entanglement:** Smaller nanostructures enable smaller spacing between

NV-centers in an eventual hardware design. The narrow gap can be exploited to ensure easier qubit entanglement operations, which are crucial also in basic quantum algorithms.

4.1.1. Analyzed Nanoparticles

The nanoparticles analyzed in this study were built using Avogadro [20], a molecule editor and visualizer designed for cross-platform used in computational chemistry, materials science, and related areas. Then the atomic structure was refined using Qbox [19], an open-source software package for atomic-scale simulations of molecules, liquids, and solids, to exploit a precise structures' relaxation that goes beyond the force field approach. This optimization cycle is crucial to obtain reliable electronic structures.
The following step-by-step process is repeated for each nanoparticle size:

1. **Supercell Selection:** The process begins by choosing a 216-atom supercell of diamond optimized with SCAN functional.

2. **Cluster Extraction:** From this supercell, we extracted the clusters of interest that were to be used in this analysis. The extracted clusters were terminated with hydrogen atoms to complete the structure of the diamondoids.
   In particular, three structures were created: $C_{35}H_{36}$, with a cage dimension of ~ 7 Å; $C_{54}H_{56}$, with a cage dimension of ~ 8 Å; $C_{69}H_{62}$, with a cage dimension of ~ 8 Å. All of them are represented in figure 1.10 (see chapter 1 at page 15).
   As it can be seen the second and the third structures do not differ much in terms of dimension, but the $C_{54}H_{56}$ was cut in a way to have a relevant deformation with respect to the usual sp^3 structure. What is expected, indeed, is to find similar electronic structures with some differences due to this deformation, since the quantum confinement effect is the same for both structures.

3. **Diamondoids Optimization:** The hydrogen-terminated clusters were then subjected to an initial optimization using the PBE functional with a tolerance of 10^{-4} $Ha/Bohr$ for the maximum force. In this initial calculation, the tolerance was kept high, to obtain precise references.

4. **NV Implantation:** After optimizing the pristine structures, the NV center was implanted into each nanoparticle. The choice of the NV position was somehow forced since the size of the nanoparticles doesn't allow exploring different configurations.

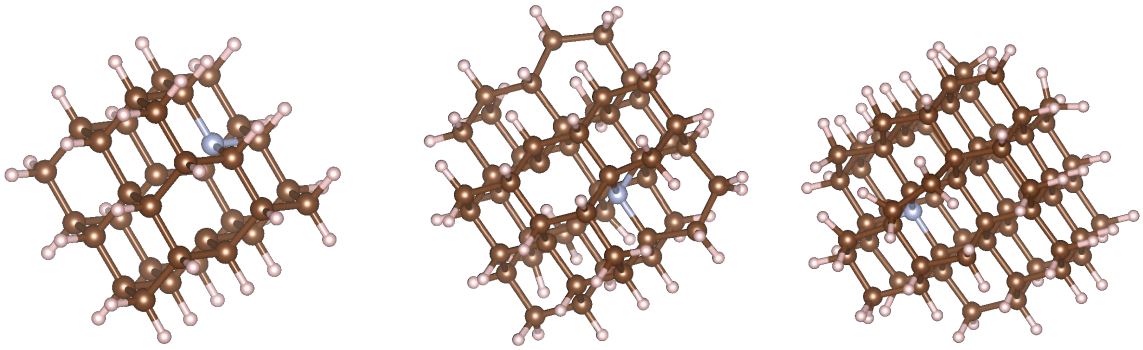

(a) $C_{33}H_{36}NV^-$ (b) $C_{52}H_{56}NV^-$ (c) $C_{67}H_{62}NV^-$

Figure 4.1: NV-diamondoids used in this work.

At the end of this step the obtained structures are $C_{33}H_{36}NV^-$, $C_{54}H_{56}NV^-$ and $C_{69}H_{62}NV^-$; they are shown in figure 4.1.

5. **NV-nanoparticles Optimization:** Following NV implantation, it was conducted a second optimization using the PBE functional with the same tolerance level.

4.2. Electronic Structures

After the nanoparticles design phase, ground state calculations including unoccupied single-electron orbitals were performed to obtain the electronic structures of the three distinct clusters.
In this section, we present the complete analysis for each cluster, beginning with the smallest one.

4.2.1. $C_{33}H_{36}NV^-$

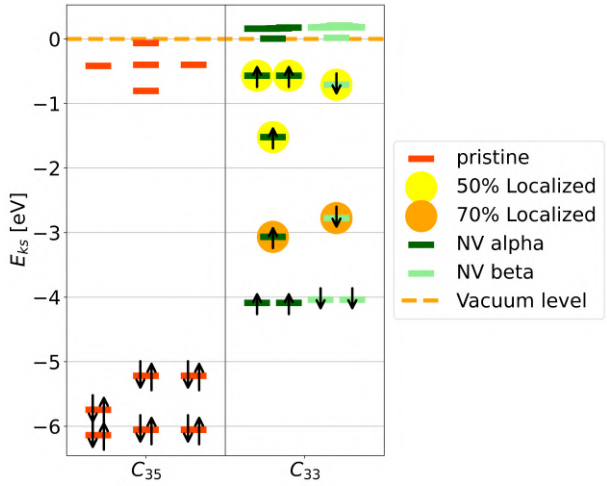

Figure 4.2: Electronic structures comparison between $C_{35}H_{36}$ (pristine) and $C_{33}H_{36}NV^-$ (NV implanted).

The electronic structure of the $C_{35}H_{36}$ cluster has some similarities with the NV-diamond electronic structure in figure 1.7a (see Chapter 1 at page 12).
In particular, the HOMO-LUMO gap of the $C_{35}H_{36}$ cluster (4.4 eV) is similar to the value for band gap of diamond (4.2 eV) obtained with the same functional [31], and is also comparable to previous studies on diamondoids [15]. As expected, this simulated gap is underestimated with respect to the experimental value (5.4 eV), because the PBE functional is known to underestimate the band gap. For this reason, every comparison with other simulations is numerically meaningful if the chosen functional is the same, otherwise, it would be useful just to compare qualitatively the results. For example, if the HSE functional is used the diamond gap is found to be 5.34 eV, in good agreement with the experimental value [34].
After implanting the NV-center, the band gap decreases to 4.2 eV. This reduction has

been verified to be independent from the energy cut-off, so it may be caused by a smaller cell than the perfect one, since, if it is taken as a reference the behavior of the $C_{69}H_{62}$ band gap in figure 3.3, it is expected that a larger cell may increase the gap slightly. We decided to continue using this cell dimension because we wanted to explore the qualitative effect of different surface terminations on the NV-nanodiamonds, for which the chosen cell dimension is sufficient.
The main issue with the $C_{33}H_{36}NV^-$ cluster is that it is characterized by a negative electron affinity, also observed previously for small clusters [15].
Electronic single-particle levels of the NV-center inside the gap can be easily identified, but the electronic structure has some differences with respect to the NV-center in diamond (in figure 1.7a, chapter 1 at page 12). In particular, for both α and β spin channels, the lower NV-localized levels, lay 1 eV above the valence band, unlike that of the NV-diamond, where they lay within the valence band.

4.2.2. $C_{52}H_{56}NV^-$

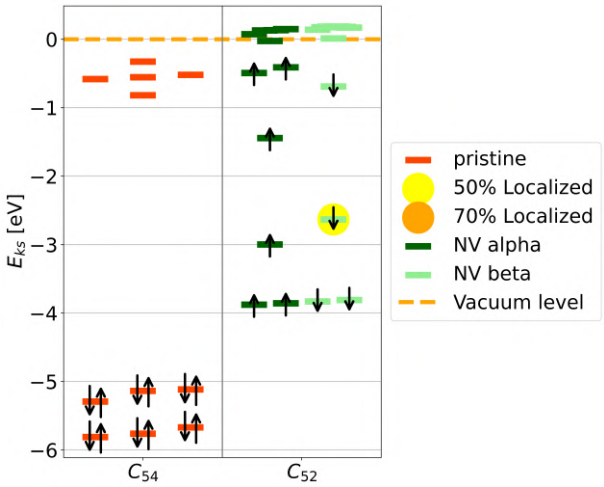

Figure 4.3: Electronic structures comparison between $C_{54}H_{56}$ (pristine) and $C_{52}H_{56}NV^-$ (NV implanted).

Though the electronic structure for this cluster is similar to the previous one, it is important to notice that, using the same criteria to assess the localization of the wavefunctions inside the NV, the electron here is less localized (around 30% in the sphere of 1.5 radius centered in the vacancy). However, the IPR approach assesses the localization of the levels that in principle should belong to the NV-center as it can be seen in figure 3.4 (see chapter 3 at page 35).

For proper understanding, it is necessary to visually investigate the wavefunctions.

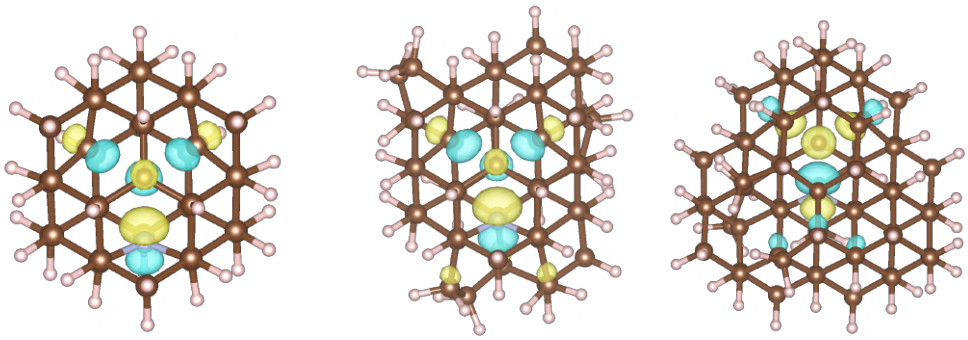

(a) $C_{33}H_{36}NV^-$ $HOMO-2$ orbital in the α spin channel (NV-localized).

(b) $C_{52}H_{56}NV^-$ $HOMO-2$ orbital in the α spin channel (not NV-localized).

(c) $C_{67}H_{62}NV^-$ $HOMO-2$ orbital in the α spin channel (NV-localized).

Figure 4.4: Orbital comparison between $C_{33}H_{36}NV^-$, $C_{52}H_{56}NV^-$ and $C_{67}H_{62}NV^-$.

It can be seen that the levels are influenced by the ring deformation and they partially localize on it. This is also the reason why the 50 % localization approach is better with respect to IPR in assessing the localization of the orbitals, as IPR is incapable to distinguish the region of the localization in the system.

4.2.3. $C_{67}H_{62}NV^-$

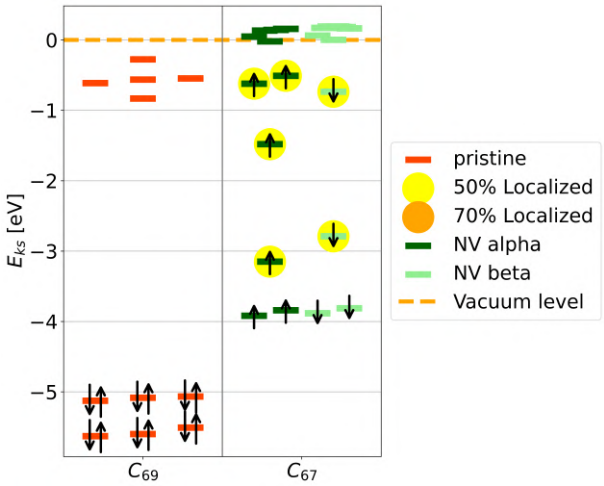

Figure 4.5: Electronic structures comparison between $C_{69}H_{62}$ (pristine) and $C_{67}H_{62}NV^-$ (NV implanted).

The $C_{67}H_{62}NV^-$ cluster shows an electronic structure almost identical to the others, with a quantitatively improved localization with respect to $C_{52}H_{56}NV^-$.
In fact, comparing the $HOMO-2$ orbital of $C_{52}H_{56}NV^-$ and $C_{67}H_{62}NV^-$ (figure 4.4), it is possible to see that the delocalization effect is induced by the ring deformation in both the structures, but the numerical approach for the orbital localization confirms that, the higher the ring deformation the more the delocalization.
We also notice that with respect to the diamond, which has a perfect C_{3v} symmetry, the degeneracy is lifted because of the broken symmetry of the system. Though the $e_{x,y}$ can still be identified by inspection (in figure 4.6), they are separated in energy.

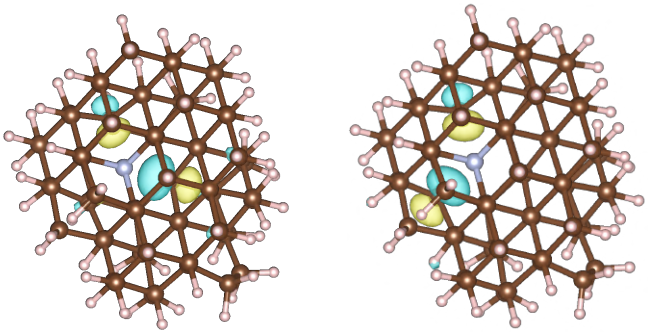

(a) $HOMO$ orbital in the α spin channel.

(b) $HOMO-1$ orbital in the α spin channel.

Figure 4.6: $e_{x,y}$ orbitals in $C_{67}H_{62}NV^-$.

4.2.4. Nanoparticles Comparison

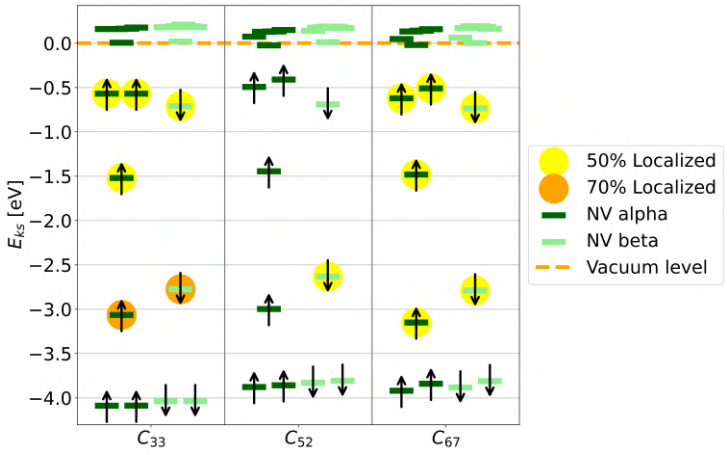

Figure 4.7: Electronic structures comparison between $C_{33}H_{36}NV^-$, $C_{52}H_{56}NV^-$ and $C_{67}H_{62}NV^-$.

Comparing the different clusters a couple of interesting effects can be underlined.
First of all, with an increase in the size of the nanoparticles, NV-localized levels approach the valence band, both in the lower α and β spin channels. This effect is consistent with the fact that by increasing the cluster size, the structure is more and more similar to the diamond, so it is expected to have similar electronic structures.
We notice a slight decrease in the gap when the particle dimension is increasing. This effect is not so pronounced because the particle dimensions are similar, but it confirms the stronger quantum confinement effect on the smallest nanoparticle, as also observed in a previous work [43]. Unfortunately the study in ref. [43] has used the B3LYP functional, so the results cannot be numerically compared.
Anyway, it is encouraging that the results obtained in this work confirm some behavior of other types of calculations found in the lacking literature on NV-center embedded in diamondoids.
In fact, all the other results that, in principle, could be taken as a reference are the output of multi-configurational studies of NV-diamond cluster models.
These calculations are based on the fact that some NV-center properties in diamond can be retrieved simulating diamond clusters instead of supercells: an optimized diamond supercell with the NV embedded into it is cut, then the multi-configurational calculation is carried out on the passivated nanoparticle without an optimization of the cluster. In this way, the symmetrical properties of the diamonds are preserved and the calculation can be carried out faster, because of the smaller number of atoms with respect to the supercell case.
For this reason, these calculations cannot be considered to make a numerical comparison, since their results refer to the diamond in its crystalline system.
Lastly, we notice that the localization in the smallest cluster is more pronounced than the localization in the largest one. This can be explained by considering the morphology of the different structures. The smallest one is composed of one complete carbon shell around the central carbon atom, so the sp^3 geometry is preserved. The other two nanostructures have an incomplete second carbon shell, so, after the relaxation, the sp^3 geometry is deformed. The effect of this deformation is more pronounced in the mid-size cluster, and in fact, the localization is worse with respect to the localization in the largest, which, however, is affected by deformed-ring delocalization.

In summary, we found that the small nanoparticles with a number of carbon atoms less than 87, which complete the second carbon shell, cannot be used for the purpose of quantum information application, since it is impossible to excite an electron localized in the

NV-center, without expelling the electron from the nanodiamond, that is a must to perform the optical readout cycle used to detect the spin state of the NV-center. However, the presence of a well-defined NV-center electronic structure inside the gap motivates us to search for some solution to engineer the nanoparticles with the aim of making them suitable for qubit use. Once all the defect levels reside within the gap, we can assume the system to show similar properties to its promising solid-state counterpart (above all the long coherence time), harnessing the advantages of the molecular environment.

5 | Surface Functionalization

A possible idea to improve the electronic properties of the NV-nanodiamonds is to functionalize the nanoparticles' surface with electron-withdrawing functional groups or atoms. As a general chemical idea, the electron-withdrawing group draws electron density toward itself, creating more space to accommodate the additional NV-electron, which is stabilized since the Coulomb repulsion decreases.
The functionalization choices have been carried out considering different aspects of changing the termination to the nanodiamonds. Among all, we considered the literature and the eventual experimental realization of nanodiamonds terminated differently from the hydrogenated one.
Henceforth, the analysis is carried out on the biggest nanoparticle ($C_{67}H_{62}NV^-$) since it is the one that would suffer the least due to the surface effect, despite we can still exploit the effects of the different terminations. Moreover, this cluster is more similar in size to the experimental realizations.

5.1. Termination Localization

To investigate the impact of the surface functionalization on the levels near the HOMO and the LUMO, we defined the measure of the localization on the single termination as the integral over the sphere centered in the central point for each functional group, in the same flavor of what we did to evaluate the localization around the vacancy.
The radius of the sphere is determined by nearest-neighbor criteria to avoid the superposition of integrals between near-terminations. The radius is chosen as the minimum between 1.5 Å and half the distances between the terminations on which the localization is calculated.
We defined the orbital to be termination-localized if at least the 50% of the wavefunction is localized on all the terminations of the nanoparticles:

$$loc_i = \sum_{k=1}^{N} \int_{V \subseteq V_{sphere,k}} |\Psi_i(\mathbf{r})|^2 dV, \tag{5.1}$$

where N is the number of functional groups in the nanoparticle.

5.2. Fluorine-terminated Nanodiamonds

The first systems that were explored are the F-terminated diamondoids. In the literature it is possible to find some experimental realization of this type of nanostructures [36][53]. In particular, in a previous work [53], the researchers were able to push the surface termination to $\frac{1}{3}$ of the total number of carbon atoms inside the structure, for this reason, the maximum number of termination in a single nanoparticle was chosen to be 17, that represents slightly less than the 30% of functionalization.

5.2.1. Design Procedure

1. **Initial Guess:** $C_{67}H_{62}NV^-$ optimized structure was chosen as the starting point. To understand which is the number of terminations on a single nanoparticle that can affect significantly the electronic properties of the system, since in the literature there are not any references for this type of nanostructures, except for the experimental work that underlines the maximum fluorination obtained on a nanodiamond. We decided to build some nanostructures with an increasing number of F-termination: $C_{67}H_{59}F_3NV^-$, $C_{67}H_{56}F_6NV^-$, $C_{67}H_{51}F_{11}NV^-$, and $C_{67}H_{45}F_{17}NV^-$.
   Moreover, we built $C_{67}F_{62}NV^-$ cluster, since, after the analysis of the previously cited nanodiamonds, it was found the extremely promising effect of the F-termination, so it was interesting to study a nanostructure in which the functionalization was pushed far beyond the actual experimental limit.

2. **Random Position Selection:** Depending on the number of the terminations we wanted to accommodate on the surface, we chose an equal number of random H positions. We began from the lowest functionalized structure ($C_{67}H_{59}F_3NV^-$), to see the effect of the termination on the NV electron. The random positions were chosen to be near the N atom or near the vacancy.

3. **Bond Lenght Adjustment:** For each F atom on the surface, the bond lengths were manually adjusted using AVOGADRO software, taking as a reference the $C-F$ bond length in $CH_3 - F$ (1.39 Å [25]).

4. **Structures Optimization:** The clusters were optimized using the PBE functional with a tolerance of 10^{-3} $Ha/Bohr$ for the maximum force. In these calculations, the tolerance was kept lower than the H-terminated structure, to speed up the process. We found that it is accurate enough to obtain reliable electronic structures.

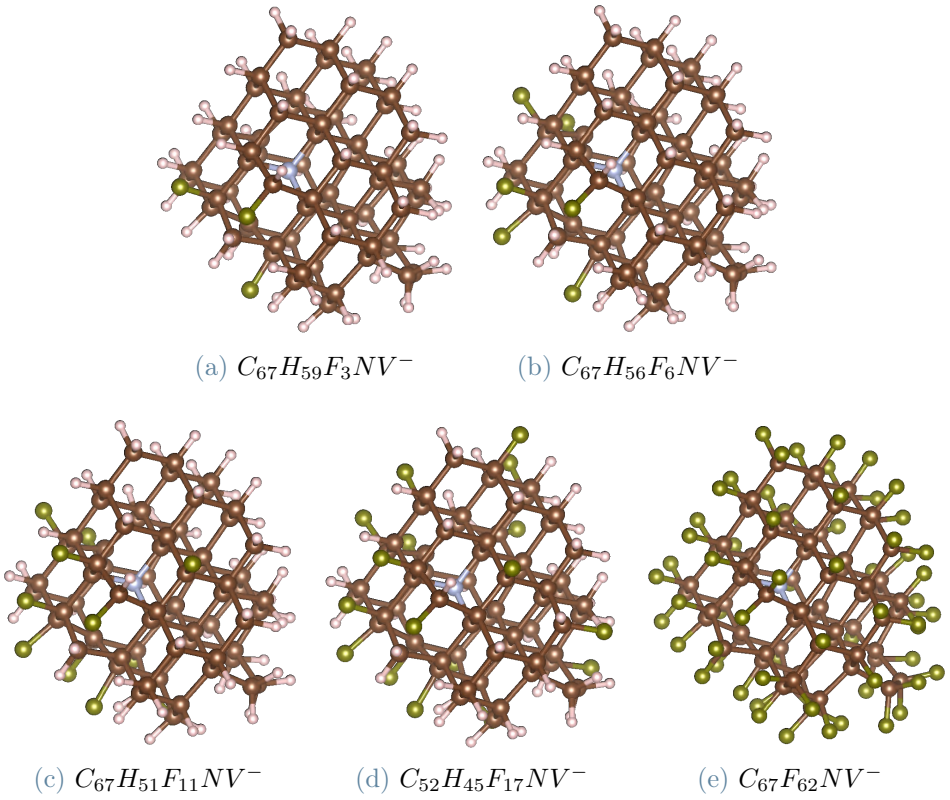

(a) $C_{67}H_{59}F_3NV^-$ (b) $C_{67}H_{56}F_6NV^-$

(c) $C_{67}H_{51}F_{11}NV^-$ (d) $C_{52}H_{45}F_{17}NV^-$ (e) $C_{67}F_{62}NV^-$

Figure 5.1: F-terminated clusters analyzed in this work.

5.2.2. Electronic Structures

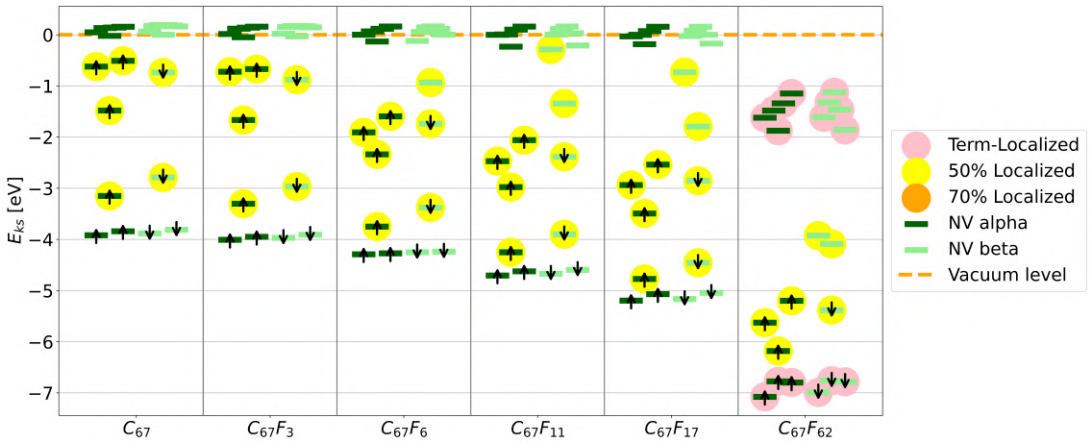

Figure 5.2: Electronic structures comparison increasing the number of F-termination on the $C_{67}H_{62}NV^-$ surface.

It can be seen that, starting from 6 F atoms, as we increase the number of terminations on the surface, the overall behavior is positive from the point of view of stabilization, and also from the point of view of the localization. In fact, the $C_{67}H_{56}F_6NV^-$ shows an increasing degree of localization for one of the unoccupied levels that start localizing inside the NV.

Then, the $C_{67}H_{56}F_6NV^-$ shows another important behavior: increasing the number of fluorine atoms the electron affinity of that NV localized empty level becomes positive, allowing to excite the electron in that level without making it dispersed in the vacuum.

For the $C_{67}H_{45}F_{17}NV^-$ cluster, we identify all the NV-like defect levels within the gap. The only difference is again the lifted degeneracy of the $e'_{x,y}$ levels due to the broken symmetry.

This latter effect is mitigated if the fluorination is complete (as in $C_{67}F_{62}NV^-$). For $C_{67}F_{62}NV^-$, though a more symmetrical nanoparticle is obtained, yet a perfect degeneracy of the various levels is not obtained due to the asymmetrical behavior of the initial diamondoid.

Moreover, in this latter nanoparticle, it can be seen that the electron affinity is remarkably large ($\sim$ 4 eV) and the separation between the HOMO and the LUMO is $\sim$ 2 eV. This behavior is crucial in the perspective of quantum information science application since it guarantees more robust excitation protocols.

It is possible to underline another behavior of increasing fluorination: the more the number of fluorine atoms, the more the occupied NV levels approach the VBM (valence band maximum) until when the lower energy ones are absorbed into the valence band, like in

the diamond.

After this first analysis, we decided to limit at 3 the number of structures analyzed for each termination, to avoid an excessive computational time consumption for this type of explorative investigation.

5.3. Hydroxyl-terminated Nanodiamonds

Now we explore the OH-termination effect on the electronic structure of nanodiamonds. This choice was motivated by a previous experiment [2], which showed the possibility of functionalizing the surface of the diamondoids with OH-groups using ozone in ambient conditions .
The OH-group is also an electron-withdrawing group, so it may stabilize the NV center electron and it is worth to explore.
$C_{67}H_{56}(OH)_6NV^-$, $C_{67}H_{51}(OH)_{11}NV^-$, and $C_{67}H_{45}(OH)_{17}NV^-$ are the three chosen nanostructures for the following analysis.

5.3.1. Design Procedure

1. **Termination Substitution:** The F-terminated nanodiamonds were taken as the starting point of the design procedure, and the F atoms were substituted with the OH groups.
   We noted that AVOGADRO placed the H atom of each group following a geometrical criteria that doesn't account for an optimized arrangement of the atoms, so the orientation of the OH bond had to be optimized, for each functional group.

2. **Bond Lenght Adjustment:** The bond lenghts were manually adjusted to the Methanol ($CH_3-(OH)$) bond lenghts ($C-O$: 1.43 Å and $O-H$: 0.96 Å [25]) for each OH group on the surface.

3. **Structures Optimization:** To avoid excessive time consumption the optimization process was carried out only on the surface of the diamondoids, thanks to the opportunity given by QBOX to freeze the atoms of the carbon cage. In this way, after fixing the OH bond lengths their orientations were optimized.

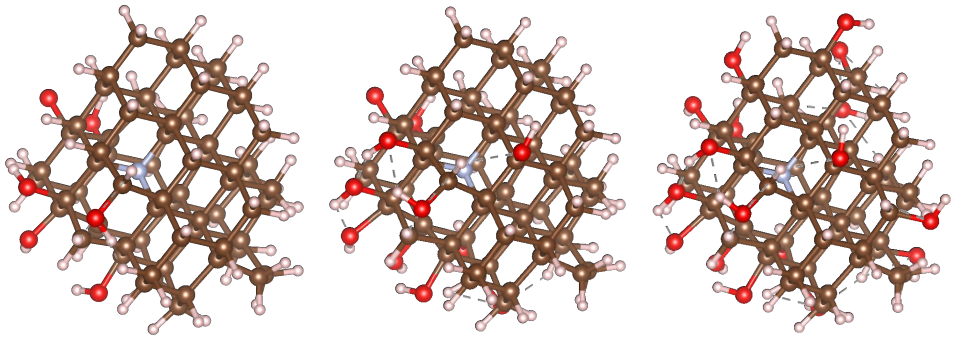

(a) $C_{67}H_{56}(OH)_6NV^-$ (b) $C_{67}H_{51}(OH)_{11}NV^-$ (c) $C_{67}H_{45}(OH)_{17}NV^-$

Figure 5.3: OH-terminated clusters analyzed in this work.

5.3.2. Electronic Structures

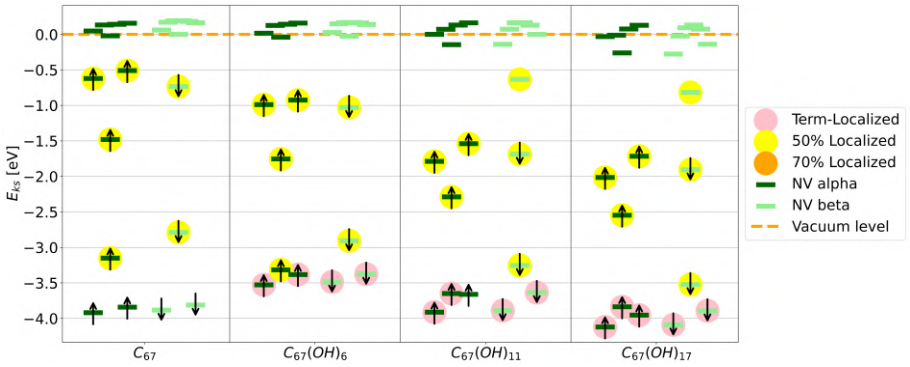

Figure 5.4: Electronic structures comparison increasing the number of OH-termination on the $C_{67}H_{62}NV^-$ surface.

We see that with an increasing number of OH-group on the surface, the overall behavior, as expected, is positive from the point of view of the stabilization. However, it is not particularly effective from the point of view of localization, since, increasing the number of OH terminations, an occupied wavefunction that was localized inside the NV starts to localize on the terminations. It is shown a localizing behavior only on one of the two empty states needed to complete the NV-electronic structure.
However the stabilizing effect of the OH termination guarantees the positive electron affinity in $C_{67}H_{51}OH_{11}NV^-$ ($\sim 0.6\ eV$) and $C_{67}H_{45}OH_{17}NV^-$ ($\sim 0.8\ eV$).

5.4. Thiol-terminated Nanodiamonds

Similar to the OH-termination, we also investigated the impact due to the SH-termination. It was expected to have a milder effect since its withdrawing capacity is less pronounced with respect to the OH-group, but it may give interesting effects due to the higher electronic cloud diffusion.
We have selected $C_{67}H_{56}(SH)_6NV^-$, $C_{67}H_{51}(SH)_{11}NV^-$, and $C_{67}H_{45}(SH)_{17}NV^-$ nanostructures for the following analysis.

5.4.1. Design Procedure

1. **Termination Substitution:** We started with the OH-terminated structures and substituted all the O atoms with the S atoms.
   We assumed that the SH bond orientations were already adjusted, thanks to their optimization in the OH-terminated nanostructures, so the surface optimization process was skipped to save computational resources.

2. **Bond Lenght Adjustment:** The bond lenghts were manually adjusted to the Methanthiol ($CH_3-(SH)$) bond lenghts ($C-S$: 1.82 Å and $S-H$: 1.33 Å [25]) for each OH group on the surface.

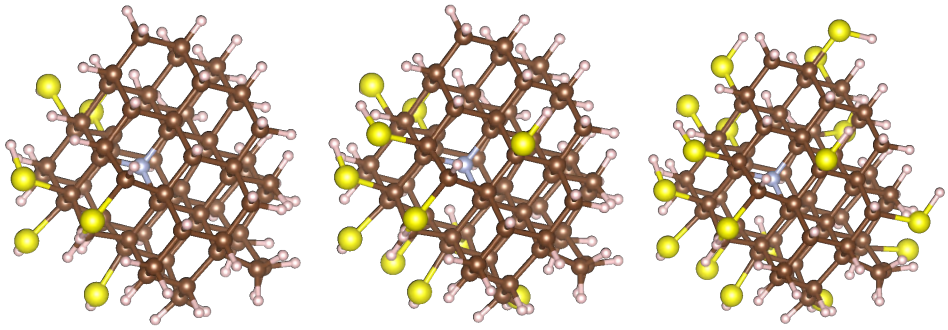

(a) $C_{67}H_{56}(SH)_6NV^-$ (b) $C_{67}H_{51}(SH)_{11}NV^-$ (c) $C_{67}H_{45}(SH)_{17}NV^-$

Figure 5.5: SH-terminated clusters analyzed in this work.

5.4.2. Electronic Structures

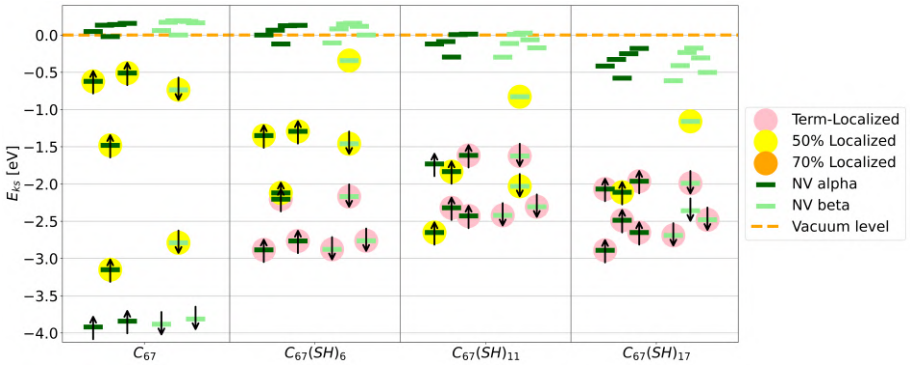

Figure 5.6: Electronic structures comparison increasing the number of SH-termination on the $C_{67}H_{62}NV^-$ surface.

We observe that with an increasing number of SH-group on the surface, the overall behavior, as expected, is again positive from the point of view of the stabilization. However, it is not desirable from the point of view of the preservation of the NV-center electronic levels inside the band gap.
First of all, the band gap in which the NV-levels are supposed to reside is reduced, e.g. for $C_{67}H_{56}(SH)_6NV^-$ it is reduced to ~ 2.6 eV.
Moreover, the defect levels within the gap become localized on the terminations showing the great impact of the SH group inside the nanoparticle.
The positive aspect is the NV-localization of an empty orbital with a significant energy decrease and the ensemble unoccupied orbitals stabilization.
It can be seen that, besides these favorable features, the overall effect of the SH termination is negative on the NV-electronic structure when the surface functionalization is increased.

5.5. Carbonyl-terminated Nanodiamonds

The last electron withdrawing termination that we analyzed is the CHO-group because it could give interesting insight due to the presence of the mesomeric resonance effect.
Since the presence of the CO double bond was expected to significantly alter the electronic structure, the decision regarding the number of terminations was made in this instance to capture the effect of the CHO group even at low functionalization concentrations.
For this reason, $C_{67}H_{59}(CHO)_3NV^-$, $C_{67}H_{56}(CHO)_6NV^-$, and $C_{67}H_{45}(CHO)_{17}NV^-$

are the structures analyzed in this section.

5.5.1. Design Procedure

1. **Termination Substitution:** We substituted the F atoms of the F-terminated nanodiamons with the CHO groups.
   These structures also show the same problem as the initial OH-terminated nanostructures, where the OH bond was wrongly oriented, so the orientation of the CO and CH bonds had to be optimized.

2. **Bond Lenght Adjustment:** The bond lenghts were manually adjusted to the Acetaldehyde ($CH_3 - (CHO)$) bond lenghts ($C - C$: 1.50 Å, $C - O$: 1.39 Å and C_H: 1.11 Å [25]) for each CHO group on the surface.

3. **Structures Optimization:** To save computational resources we carried out the optimization process only on the surface of the diamondoids.

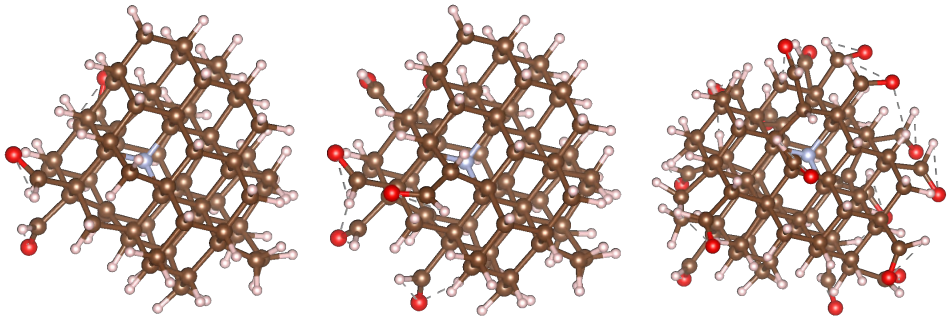

(a) $C_{67}H_{59}(CHO)_3NV^-$ (b) $C_{67}H_{56}(CHO)_6NV^-$ (c) $C_{67}H_{45}(CHO)_{17}NV^-$

Figure 5.7: CHO-terminated clusters analyzed in this work.

5.5.2. Electronic Structures

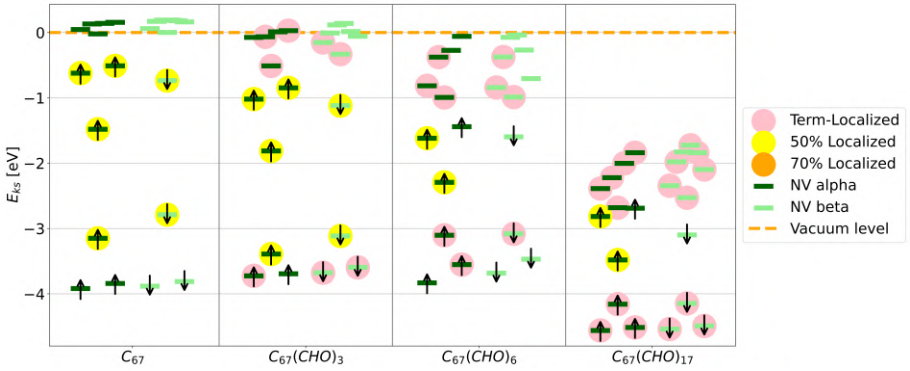

Figure 5.8: Electronic structures comparison increasing the number of CHO-termination on the $C_{67}H_{62}NV^-$ surface.

We notice that already in $C_{67}H_{59}(CHO)_3NV^-$ the defect levels inside the gap (that is reduced to ~ 3.0 eV) are not preserved and some wavefunctions start to localize on the terminations.
This behavior is accentuated when the functionalization is increased and becomes particularly evident in the $C_{67}H_{45}(CHO)_{17}NV^-$ structure.
In this latter structure, it is clear the huge influence of the termination in terms of localization behavior, in fact almost all the levels are localized on the CHO-group.
The explanation of this behaviour can be retrieved by computing the Maximally Localized Wannier Functions [39], since, once controlled by inspection, they reveal the shape of the orbitals localized on the termination: those wavefunctions (some of them in figure 5.9) are similar to the classic π-orbital shape (bonding and anti-bonding), and it is known that in a system rich in π-orbitals the gap is extremely narrow.

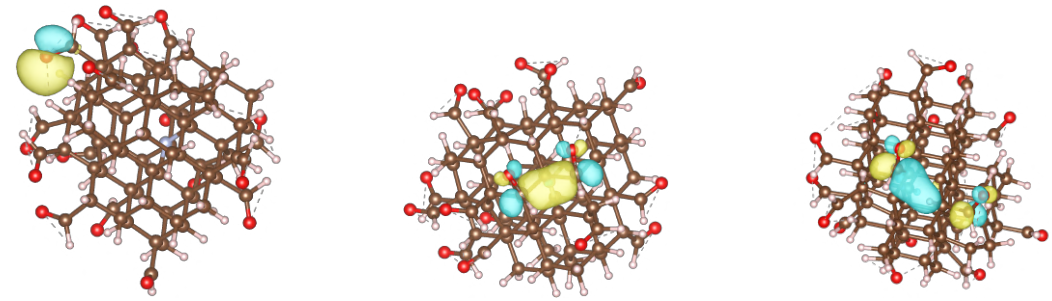

(a) $C_{67}H_{45}(CHO)_{17}NV^-$ $HOMO-3$

(b) $C_{67}H_{45}(CHO)_{17}NV^-$ $LUMO$

(c) $C_{67}H_{45}(CHO)_{17}NV^-$ $LUMO+1$

Figure 5.9: $C_{67}H_{45}(CHO)_{17}NV^-$ Maximally Localized Wannier Functions.

However, it is important to notice the massive stabilization of the empty levels, which creates a more stable particle in the excited states, in fact, the electronic affinity is ~ 2.6 eV in $C_{67}H_{45}(CHO)_{17}NV^-$, but it is also significant in $C_{67}H_{51}(CHO)_{11}NV^-$ (~ 1.0 eV).

5.6. Termination Comparison

After having described all the terminations in detail, it is important to understand the differences between each of them. For this sake, we compare the different systems to extract deeper insight into the effect of the terminations.

5.6.1. Spin Accumulation Analysis

The first simple analysis that was performed on the terminated-nanoparticles to understand their differences is the evaluation of each termination effect on the spin accumulation in the ground state.
It was expected to find an increase in the localization of the spin accumulation inside the NV for each electron withdrawal groups since the extra spin can accommodate better due to a more favorable Coulomb potential.
The spin accumulation is an index that shows clearly where the extra spin is distributed inside the nanoparticle, so, after having subtracted the two spin densities and using the localization approach described in chapter 3, the localization factor has been calculated and the results are shown in figure 5.10.

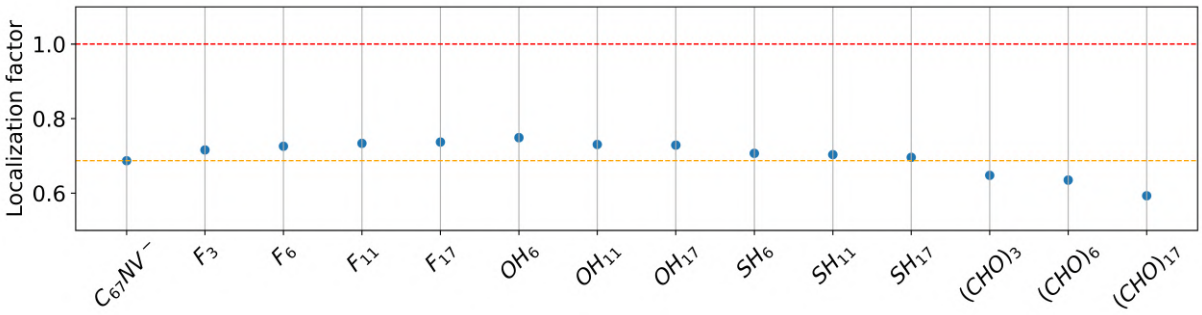

Figure 5.10: Spin accumulation in each structure with different termination.

It is clear that in the ground state, the effect of the terminations is overall slightly positive, except for the CHO termination. Evidently, the CHO termination is not promising for

the target applications.

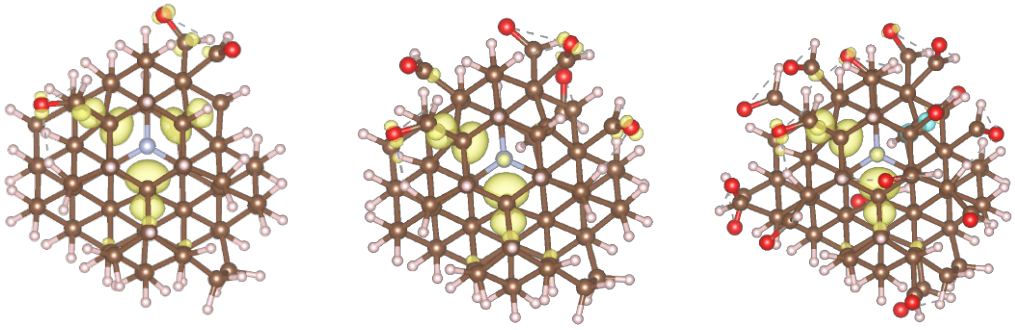

(a) $C_{67}H_{59}(CHO)_3NV^-$ spin accumulation (b) $C_{67}H_{56}(CHO)_6NV^-$ spin accumulation (c) $C_{67}H_{45}(CHO)_{17}NV^-$ spin accumulation

Figure 5.11: Spin accumulation in the CHO-terminated clusters.

Visual inspection of the spin densities (in figure 5.11) makes clear that the spin accumulation behavior is dominated by the CHO-group distribution on the surface.
So when the functionalization increases, the additional electron is attracted towards the terminations, provoking a decrease in the spin accumulation, which also becomes negative in a lobe when the functionalization is pushed to 17 CHO-groups.

5.6.2. Electronic Structure Comparison

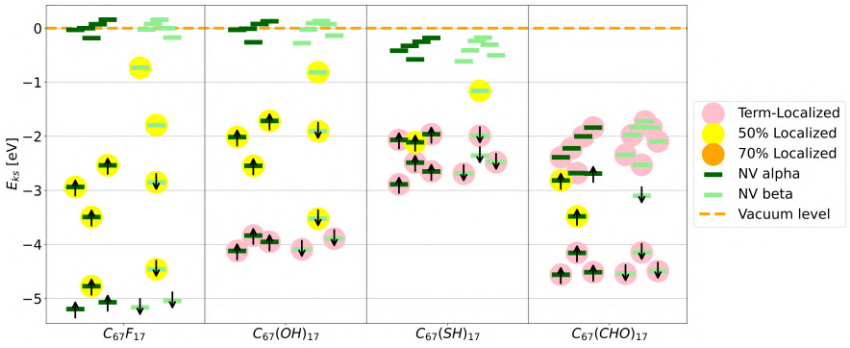

Figure 5.12: Electronic structure comparison between the structures terminated with 17 functional groups.

In this analysis, to understand the peculiar effect of each termination it is considered only the highest-functionalized nanoparticles for each group.

It is clear that the most effective termination in terms of combining localization and stabilization is the fluorine, but SH and CHO show interesting behavior from the point of view of empty levels general stabilization.
For this reason, in the following section, we explore the combined effect of F with SH or CHO, to understand if it is possible to exploit the favorable behavior of each termination.

5.6.3. Double-terminated Nanodiamonds

The structures built and analyzed in this section are summarized in table 5.1.

$F-CHO$-terminated	$F-SH$-terminated
$C_{67}H_{45}F_{16}(CHO)_1NV^-$	$C_{67}H_{45}F_{16}(SH)_1NV^-$
$C_{67}H_{45}F_{15}(CHO)_2NV^-$	$C_{67}H_{45}F_{15}(SH)_2NV^-$
-	$C_{67}H_{45}F_{14}(SH)_3NV^-$
-	$C_{67}H_{45}F_{12}(SH)_5NV^-$

Table 5.1: Double-functionalized nanodiamonds analyzed in this section.

Design Procedure

The design procedure for each of these double-terminated nanoparticles is similar to the design of the single-terminated structures, and, to save computational resources, the optimization was not carried out, since this analysis was performed to obtain a tentative idea of the combined terminations effect.

1. **Termination Substitution:** $C_{67}H_{45}CHO_{17}NV^-$ was taken as the starting point for the $F-CHO$-terminated nanostrcutures, since we can assume to have the CHO bond directions optimized. In this way, it was possible to substitute the CHO groups with the F atoms. We repeated the same procedure for the $F-SH$-terminated nanostructures, starting from $C_{67}H_{45}SH_{17}NV^-$.

2. **Bond Lenght Adjustment:** We adjusted the bond lenghts (CF) as described earlier.

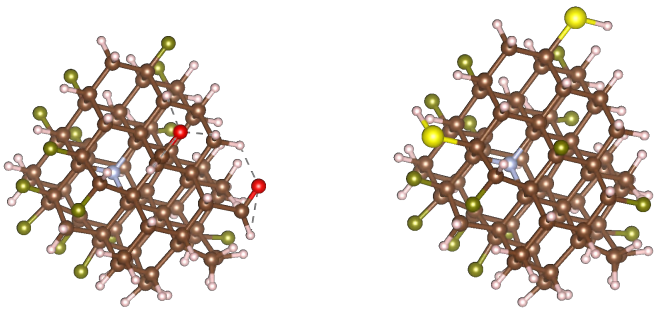

(a) $C_{67}H_{45}F_{15}(CHO)_2NV^-$

(b) $C_{67}H_{45}F_{15}(SH)_2NV^-$

Figure 5.13: Two of the double-terminated clusters analyzed in this work.

Electronic Structures

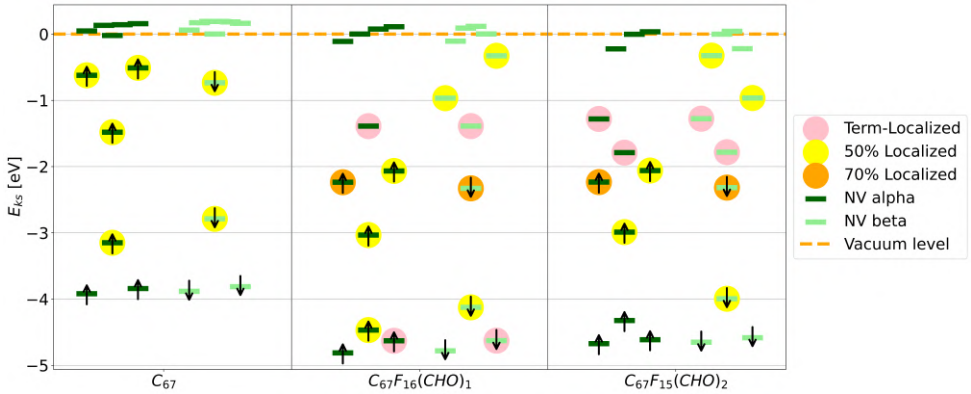

(a) Electronic structure comparison between the structures terminated with F and CHO functional groups.

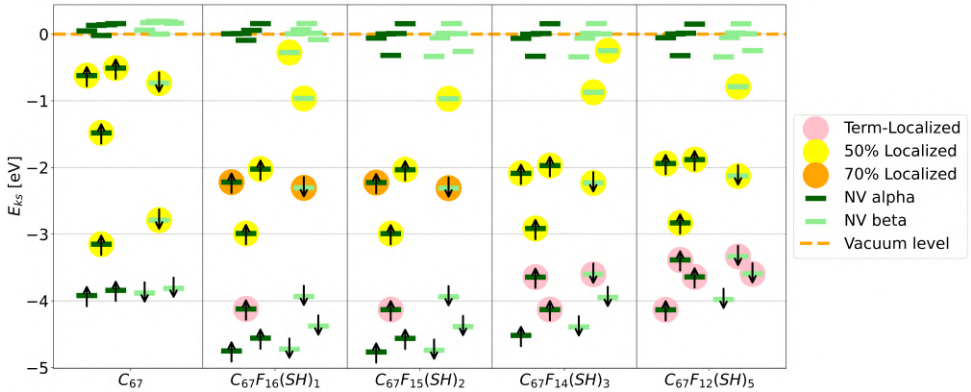

(b) Electronic structure comparison between the structures terminated with F and SH functional groups.

Figure 5.14: Electronic structures of all the double-terminated structures analyzed in this work.

The electronic structures of the various clusters show that the effect of the combined terminations is undesirable. In particular, a single CHO group combined with 16 F atoms doesn't preserve the NV electronic structure, since it introduces two empty termination-localized states within the NV-levels. On the other hand, the SH termination is not as impactful as the CHO group, but the trend is again detrimental.
In both types of structures, the termination-localization effect and the gap reduction effect are way more pronounced than the stabilization effect.
In conclusion, we can confirm that the most effective termination is the F-termination alone.

5.6.4. Radial Potential Calculation

To retrieve the crucial information that can explain the different effects of each termination we calculated the radial potential starting from the barycentre of the nanoparticles.
QBOX code provides the Coulomb potential as a volumetric file, so to evaluate the mean potential at a certain radius we integrated the potential within two consecutive spherical surfaces:

$$\sigma(\mathbf{r}) = \frac{1}{V_{sphere}(\mathbf{r}) - V_{sphere}(\mathbf{r}-\mathbf{dr})} \int_{V \subseteq (V_{sphere}(\mathbf{r}) - V_{sphere}(\mathbf{r}-\mathbf{dr}))} V(\mathbf{x},\mathbf{y},\mathbf{z}) dV, \tag{5.2}$$

where dr is the thickness of each spherical shell in which the potential was integrated.

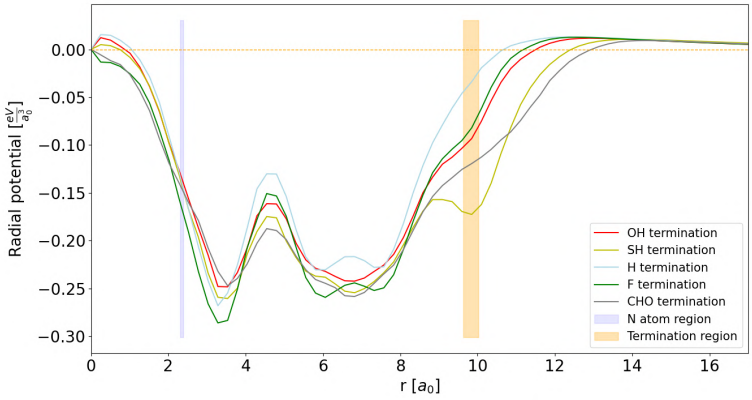

Figure 5.15: Radial potential comparison between each termination, with a focus in the NV region.

In the region around the N atom, the potential has a minimum at a radius corresponding to the distance of the vacancy from the center of the nanoparticles.

Evidently, the only termination that guarantees an effective stabilizing behavior for the electron within the vacancy is the F-termination. All the other terminations perform even worse than the H-terminated structure.
The reduced Coulomb repulsion stabilizes the unoccupied levels of the nanodiamonds with different terminations, as evident from the radial Coulomb potential, which is highest for the H-terminated nanodiamond.
This evidence underlines the importance of the chemical concept of withdrawing/donating functional group, since the stabilization process occurs due to the modification of the coulomb potential, without the necessity to include electron exchange and correlation contributions.
On the other, it is important to notice that the chemical intuition fails with the stabilization order of OH and SH, since it is expected that OH stabilize more than SH.
To investigate this last consideration on chemical intuition a more profound analysis of the CO bond and CS bond was performed, to understand the reason for the intuition failure.

Bond Axis Analysis

To reveal the reason why the SH group stabilizes better the electronic structure with respect to the OH group, regardless of the less electronegativity, we calculated the linear charge density along the CO bond axis and the CS bond axis.
From the computational point of view, we have integrated the charge density volumetric file slice by slice in a cylinder of 2 Å radius, to ensure the inclusion of all the electrons near the O/S atom.

$$\lambda(\mathbf{z}) = \int_{V \subseteq (V_{slice}(\mathbf{z}|\mathbf{dz}))} \rho(\mathbf{x}, \mathbf{y}, \mathbf{z}) dV, \tag{5.3}$$

where dz is the thickness of each cylindrical slice in which the charge density ρ is integrated.

The linear charge density was calculated for each bond in $C_{69}H_{45}(OH)_{17}NV^-$ and $C_{69}H_{45}SH_{17}NV^-$, then the average profile was evaluated and it is shown in figure 5.16.

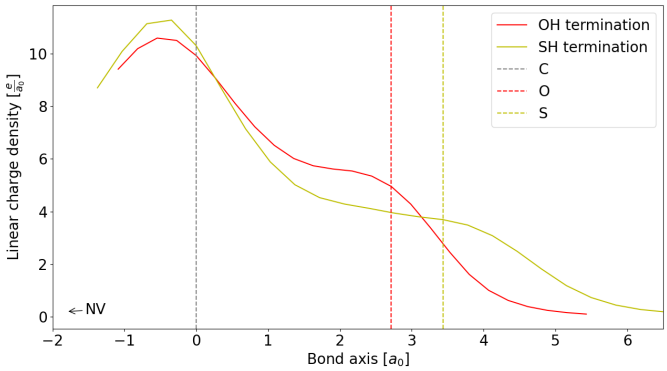

Figure 5.16: Linear density comparison along the bond axis between OH termination and SH termination.

The linear charge density profiles show that the SH termination stabilizes better the nanoparticle electronic structure due to the more diffused $3sp^3$ orbitals of the S atom with respect to the $2sp^3$ orbitals of the O atom (both atoms in a C_{3v} symmetrical environment hybridize their s and p orbitals to obtain sp^3 hybrid orbitals), and the CS bond length that is longer than the CO bond length.
For these reasons the charges are better accommodated in the SH terminations.

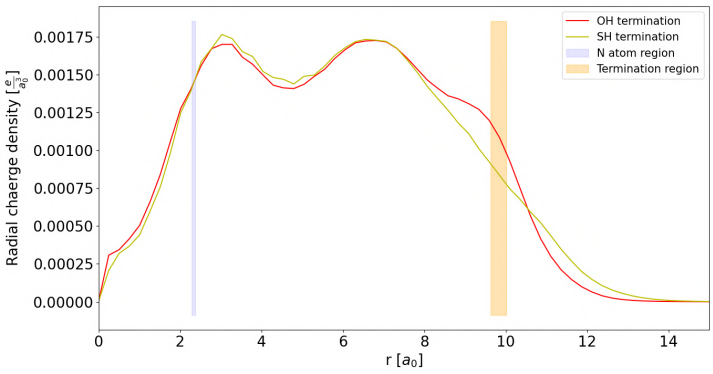

Figure 5.17: Radial density comparison between OH termination and SH termination.

$$\theta(\mathbf{r}) = \frac{1}{V_{sphere}(\mathbf{r}) - V_{sphere}(\mathbf{r}-\mathbf{dr})} \int_{V \subseteq (V_{sphere}(\mathbf{r}) - V_{sphere}(\mathbf{r}-\mathbf{dr})} \rho(\mathbf{x},\mathbf{y},\mathbf{z}) dV, \tag{5.4}$$

Moreover, this last consideration becomes even more evident if it is evaluated the radial charge density (in figure 5.17), which is calculated with the same approach of the radial

potential. In fact, it is clear the larger spacing between charges in the SH-terminated structure.

During the exploration of the different terminations we have found that all the electron-withdrawing groups stabilize the unoccupied levels, but only the F-termination does not damage the defect levels within the gap. In fact, all the other terminations localize the spin density slightly outside the NV or delocalize some of the NV-localized levels, which is undesirable for applications.
In conclusion, we want to underline that the promising result for the F-terminated nanostructures, which is ideal for quantum information science applications, may push the research towards smaller cluster functionalization, to understand if the termination effect is strong enough to counterbalance the negative electronic affinity of these clusters.

6 | Nanodiamonds Molecular Crystals [1]

This last chapter on results aims to investigate the behavior of the nanodiamonds' electronic structure when they crystallize and are pressurized.
We have decided to study this system because it approaches the idea of building a proper quantum hardware, in which qubits are not isolated, but they can be entangled, and, in general, interact with each other.
Moreover, in such a system it is also possible to explore the effect of macroscopic variables such as temperature and pressure. In fact, different works showed the effectiveness of pressure in controlling the electronic structure of the crystals on which it acts, and in particular on the diamond electronic structure [11].
In fact, it was demonstrated through DFT-GGA calculations that, under extreme pressure conditions ($1,100\ GPa$) the gap in the diamond increases from $4.4\ eV$ to $6.9\ eV$ [11].
In this context could be interesting to understand whether the diamondoid molecular crystal shows the same behaviour since in that case, it would be possible to isolate the NV-levels well inside the gap.
Moreover, it would be also interesting to investigate the localization properties of each orbital when it is put under pressure.
On the other side of the picture, since the population of the different phonon modes can have a significant impact on our system's electronic structure, the effect of temperature, which is important to study in the context of ambient-temperature qubit, has to be examined. [16][17]
In this chapter, we analyze both the $C_{67}H_{62}NV^-$ and $C_{67}H_{45}F_{17}NV^-$ when they form a BCC no-point symmetric molecular crystal.

[1] This chapter has been developed within the context of the Honours Programme "Scientific Research in Industrial Engineering".

6.1. Crystal Structure Design

Designing the crystal structure for this type of molecule is not straightforward due to its inherent asymmetry. In fact, the geometry choice for the crystal symmetry was constrained by the incompatibility between the proper representation of a BCC crystal structure (or whatever else basic crystal structure) and the computational power needed to simulate the system.

We used PyXTAL [14], in combination with VESTA [40] to build the primitive cell. Through PyXTAL it was possible to determine that the number of $C_{67}H_{62}NV^-$ needed in a single cell to replicate a BCC system is 96, which clearly requires a huge cell parameter and $96 \times 131 = 12576$ atoms to be simulated.

This number of nanoparticles is needed to guarantee the symmetry requirements (both lattice symmetry and point symmetry) of the BCC crystal structure.

Considering that in a BCC unit cell are contained two equal elements (1 in the center and 1/8 for each vertex), each nanoparticles aggregate is composed of 48 $C_{67}H_{62}NV^-$ nanodiamonds.

It was expected that for the $C_{67}H_{45}F_{17}NV^-$ molecular crystal, these numbers increase, due to the asymmetric behavior introduced by the differences in the terminations.

For this reason, we decided to simulate a BCC crystal structure that respects only the lattice symmetry and not the point symmetry.

For this sake, we built the primitive cell for the BCC structure, which is a triclinic cell with $a = b = c$ and $\alpha = \beta = \gamma = 109.4\overline{6}^\circ$. To simulate the effect of different values for the hydrostatic pressure, the cell parameter was chosen equal to 24, 21, 18, 15, 12 Å, then the respective hydrostatic pressure was obtained through the stress tensor calculation performed with QBOX.

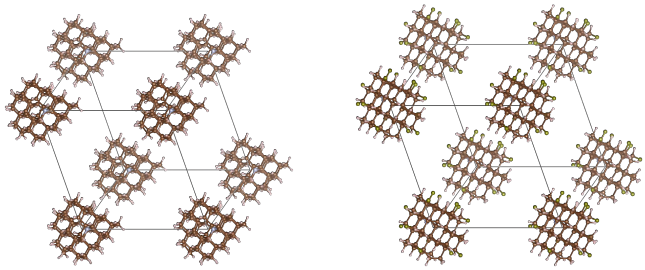

(a) $C_{67}H_{62}NV^-$ unit cell. (b) $C_{67}H_{45}F_{17}NV^-$ unit cell.

Figure 6.1: BCC molecular crystal unit cell with cell parameter $a = 18$ Å.

We chose to simulate the BCC crystal structure since some diamondoids crystalize with this symmetry [52]. The violated point symmetry does not affect drastically the general result of the calculations.
All the crystal systems obtained were optimized with a force tolerance of 10^{-3} $Ha/Bohr$.

6.2. Electronic Structure

In this section, we describe the electronic structures of the two different crystalline systems, in order to underline differences and common characteristics.

6.2.1. $C_{67}H_{62}NV^-$ Molecular Crystal

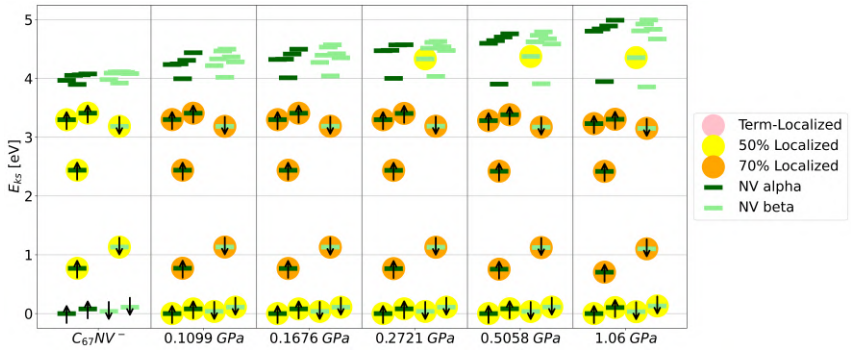

Figure 6.2: Electronic structures comparison for the $C_{67}H_{62}NV^-$ BCC molecular crystal under different pressures.

If we consider the $C_{67}H_{62}NV^-$ in the 60 $Bohr$ cell as the isolated nanoparticles we can observe that, once the electronic structures are aligned at the VBM (Valence Band Maximum), the conduction band show an overall energy increasing behavior.
However, since the CBM (Conduction Band Minimum) seems to be stationary in energy, it cannot be stated that the VBM-CBM gap is increasing as well. The behavior of the CBM will be investigated later, since if it is excluded, it can be shown that the VBM-(CMB+1) gap is gradually increasing with the pressure, as was expected considering the gap behavior in the diamond under pressure [11].
The pressures reached in these simulations are far below the maximum pressure reached in other computational studies [11], and in experimental setup [52], making these results reliable and meaningful also for practical applications.

Although we demonstrated the efficiency of the pressure in increasing the gap in which the NV-levels could reside, we noticed that the NV defect levels are not complete: one of the unoccupied levels becomes NV-localized and grossly respect the e' orbital shape, as it can be seen in figure 6.3, but the CBM lays in between the HOMO and this level. Moreover, the other unoccupied level needed to complete the NV-center electronic structure is not found to be localized.

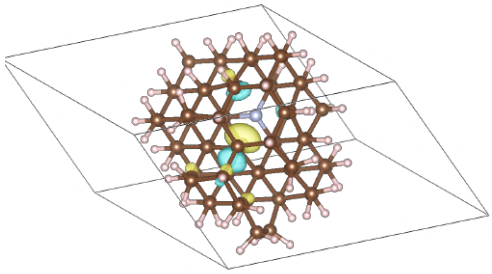

Figure 6.3: $C_{67}H_{62}NV^-$ $LUMO+1$ at 1.06 GPa.

For these reasons, the $C_{67}H_{62}NV^-$ molecular crystal cannot be exploited to implement quantum hardware.
The second important finding is that the NV localized levels become even more localized (70% of the wavefunctions are inside the 1.5 Å radius sphere centered in the vacancy), which is beneficial from the point of view of applications.
Moreover, the valence band levels become localized inside the vacancy, but this doesn't affect any states-controlling protocol, since it is important to understand that the localization-inside-the-vacancy criteria is not effective on the real properties of the system, it is a measure to evaluate quantitatively what is the spatial diffusion of the orbitals, that can be evaluated by inspection.

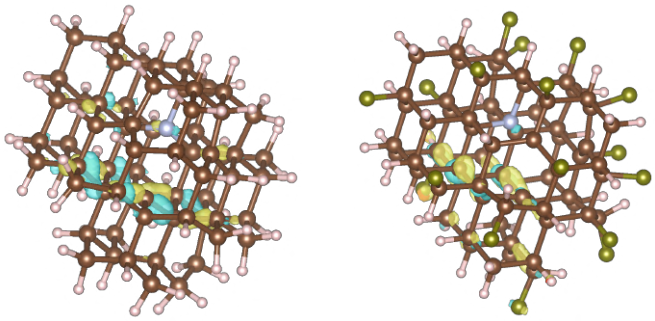

(a) $C_{67}H_{62}NV^-$ $HOMO-5$ in the α-spin channel at 1.06 GPa.

(b) $C_{67}H_{45}F_{17}NV^-$ $HOMO-5$ in the α-spin channel at 1.67 GPa.

Figure 6.4: Localized orbitals in the valence band for the molecular crystals with cell parameter $a = 12$ Å.

In fact, proceeding in this direction, we analyzed the valence-band-localized orbitals. These levels are localized outside the NV-center, in particular, they are localized on the bonds surrounding the vacancy, so they are included in the 1.5 Å sphere used to evaluate the localization.

6.2.2. $C_{69}H_{45}F_{17}NV^-$ Molecular Crystal

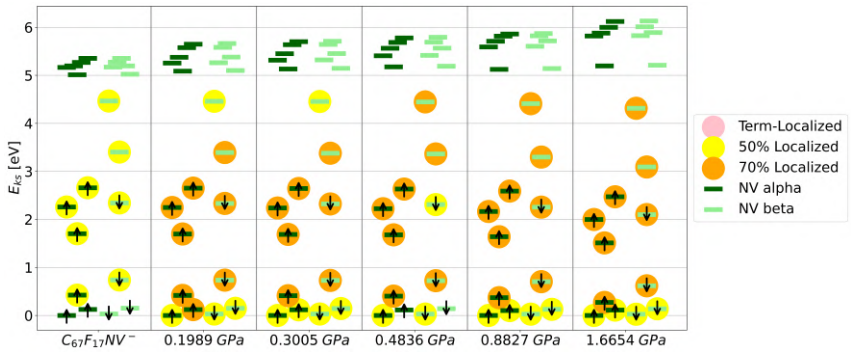

Figure 6.5: Electronic structures comparison for the $C_{67}H_{45}F_{17}NV^-$ BCC molecular crystal under different pressures.

The electronic structures of $C_{67}H_{45}F_{17}NV^-$ and $C_{67}H_{62}NV^-$ molecular crystals behave similarly with increasing pressure: NV-levels localization increases, valence band localizes, and conduction band energy increases as well (with CBM stationary).
In this case, the pressure effects are favorable since the NV electronic structure is still complete but improved in localization. We note that here the separation between the

highest in energy NV-localized empty orbitals and the CBM is of 0.9 eV, which is positive for practical quantum protocol implementation since the risk of exciting one of the NV-electrons to a delocalized level is reduced.
It is now imperative to comprehend the underlying reasons for the pressure's influence on the electronic structures of nanodiamonds.
The localization effect can be understood qualitatively considering that if the distance between the nanoparticle decreases the Coulomb repulsion between the electronic cloud increases, leading to a higher electron localization on the nanoparticle.
On the other hand, it is not so straightforward to understand the reason for the increasing energy for the conduction band.

6.2.3. Empty Levels Behaviour

The investigation of the conduction band levels properties starts from a phenomenological observation, in fact, it can be shown that the energy of the conduction band levels (excluding the CBM) behaves as a $\frac{1}{L^2}$ (in figure 6.6 and 6.7) as a first approximation if as L is taken the cell parameter.
So, we assume this tendency to be a good approximation to describe the effect of pressure on the molecular crystal.
This phenomenological intuition has a profound physical meaning since it resembles the energy behavior of a particle in a box model.
This simple model serves as a foundational example of quantization in quantum mechanics and helps to understand the quantized energy levels and wave functions associated with confined particles.
It describes the energy levels of a particle when it is confined within a cubic box, and shows that the energy dependence on the box dimension (confinement length) is proportional to $\frac{1}{L^2}$ where L is the confinement length. In fact, if it is considered a $2D$ box (for simplicity and to visualize the wavefunctions), the associated energy eigenvalues follow the equation:

$$E_{n_x,n_y} = \frac{\hbar^2\pi^2}{2mL^2}(n_x^2 + n_y^2) \tag{6.1}$$

where n_x and n_y are positive integers respectively representing the quantum numbers in the x and y dimensions, and the corresponding wave functions, $\psi_{n_x,n_y}(x,y)$, are:

$$\psi_{n_x,n_y}(x,y) = \sqrt{\frac{4}{L^2}} \sin\left(\frac{n_x\pi x}{L}\right) \sin\left(\frac{n_y\pi y}{L}\right) \tag{6.2}$$

The wavefunctions are represented in the range from 1 to 3 for each quantum number in figure 6.8.

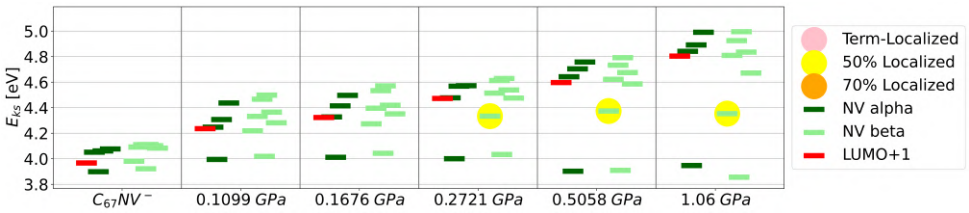

(a) $C_{67}H_{62}NV^-$ conduction band.

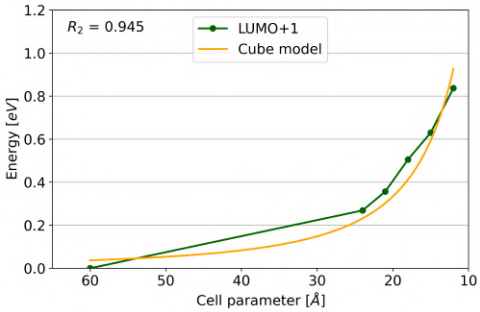

(b) $C_{67}H_{62}NV^-$ $LUMO+1$ behaviour with $\frac{1}{L^2}$ fit.

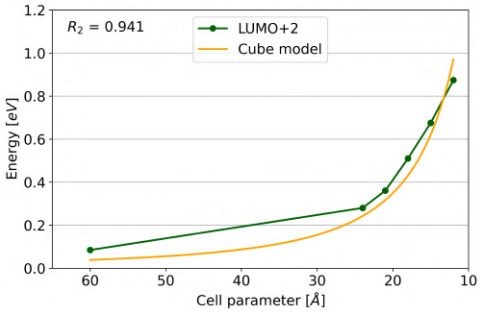

(c) $C_{67}H_{62}NV^-$ $LUMO+2$ behaviour with $\frac{1}{L^2}$ fit.

Figure 6.6: Conduction band energy behaviour in the $C_{67}H_{62}NV^-$ molecular crystals.

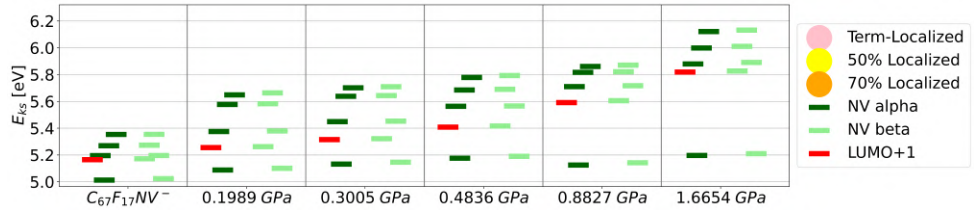

(a) $C_{67}H_{45}F_{17}NV^-$ conduction band.

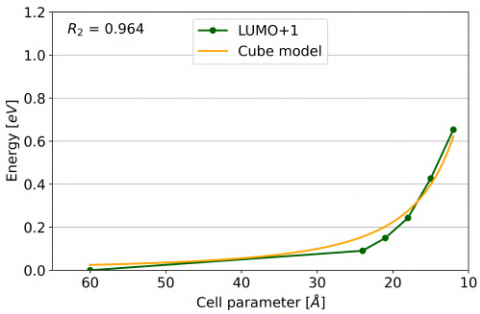

(b) $C_{67}H_{45}F_{17}NV^-$ $LUMO+1$ behaviour with $\frac{1}{L^2}$ fit.

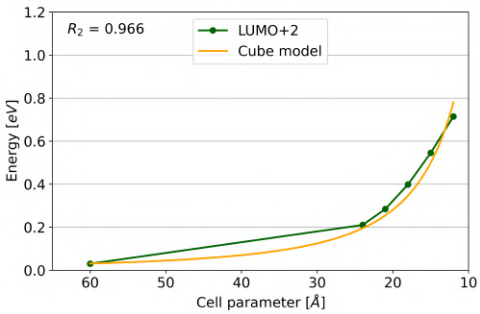

(c) $C_{67}H_{45}F_{17}NV^-$ $LUMO+2$ behaviour with $\frac{1}{L^2}$ fit.

Figure 6.7: Conduction band energy behaviour in the $C_{67}H_{45}F_{17}NV^-$ molecular crystals.

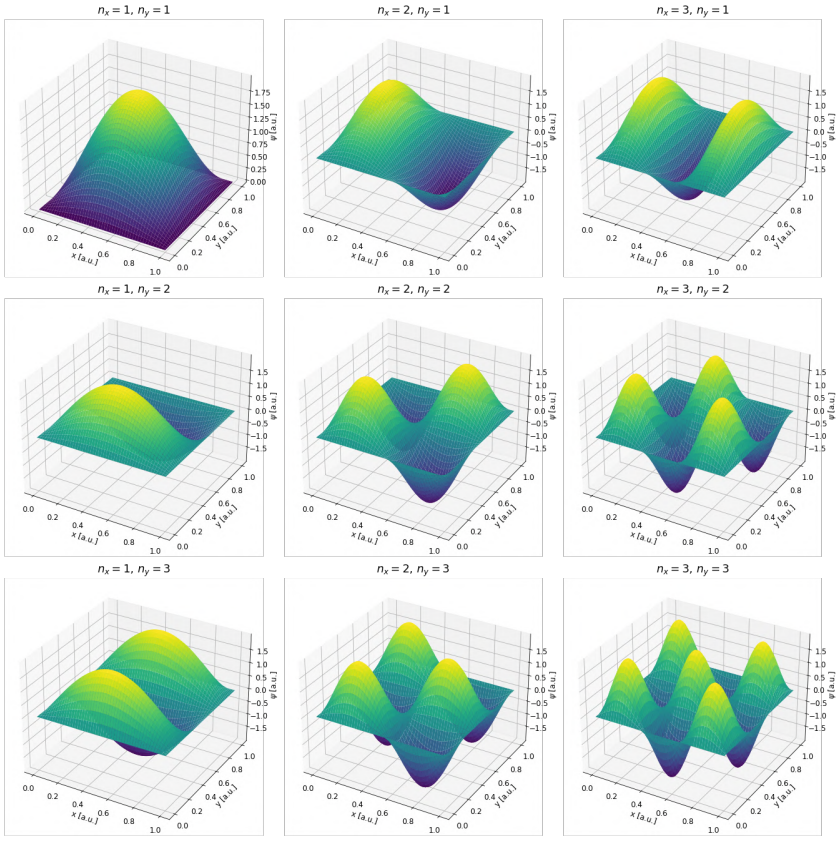

Figure 6.8: Wavefunctions for the 2D particle in a box model, with each quantum number ranging from 1 to 3.

This means that it is interesting to evaluate if there exists a confinement length for those orbitals that show the $\frac{1}{L^2}$ behavior.
For this reason, if the $LUMO + 1$ orbital is taken as a reference, it is possible to show that increasing the pressure at a certain hydrostatic stress the orbital, which is in normal condition localized outside the nanoparticle, collapses in between two consecutive nanoparticles, as it can be seen in figure 6.9.
After the collapse, the confinement length is well defined as the distances between the two nanoparticles, which clearly decreases as the cell parameter.
This simple model could help to understand the quantum confinement effect on the conduction band orbitals, but it cannot be rigorously mathematically formulated for different reasons.
First of all, the confinement length is not easy to be defined, because of a shape effect that can be thought as a sort of orbital fluidity, since the wavefunction doesn't remain fixed in the direction between the nanoparticles, and changes its shape continuously during the pressurization process, as it can be observed in figure 6.9.

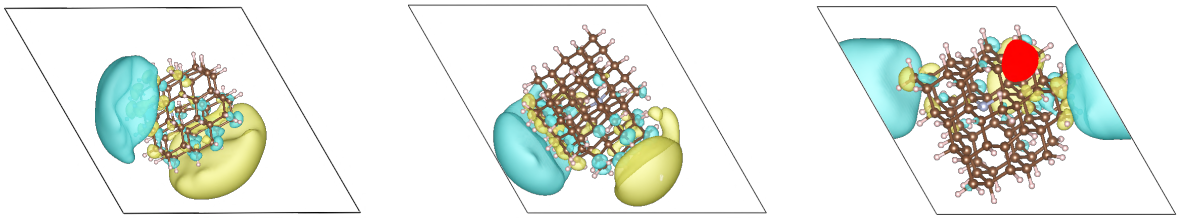

(a) $C_{67}H_{62}NV^-$ $LUMO+1$ in the α-spin channel at 0.168 GPa.

(b) $C_{67}H_{62}NV^-$ $LUMO+1$ in the α-spin channel at 0.272 GPa.

(c) $C_{67}H_{62}NV^-$ $LUMO+1$ in the α-spin channel at 0.508 GPa.

Figure 6.9: $LUMO+1$ instability leading to collapse in between the $C_{67}H_{62}NV^-$ nanoparticles.

Another important evidence is that the orbital is not completely localized in between the nanoparticles, but has some important contributions localized on the nanoparticles, that do not perceive the effect of the pressure.
Then, the most impactful effect on this simple model is the presence of interactions between the conduction band levels and all the electronic and nuclear states in the particle itself, which in a pure particle-in-a-box approach are not considered.
Besides this issue, it is important to understand that this simple model allows to explain the behavior of the conduction band levels from a quantum confinement perspective.

The last unresolved question is the behavior of the CBM (α spin channel $LUMO$ in the $C_{67}H_{62}NV^-$ crystal and in the $C_{67}H_{45}F_{17}NV^-$ crystal); by inspection, we can show that the morphology of this level is not affected by the pressure, since it is not massively localized outside the nanoparticle, but it is relatively localized on the nanoparticle, as it can be seen in figure 6.10 and in figure 6.11. Comprehensibly, the incomplete localization on the nanoparticle provokes the energy fluctuation in the CBM, especially in the $C_{67}H_{45}F_{17}NV^-$ crystal, since it is clear the presence of an orbital lobe outside the nanoparticle, which perceives intensively the pressure effect.

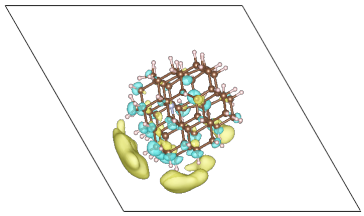

(a) $LUMO$ in the α-spin channel at 0.168 GPa.

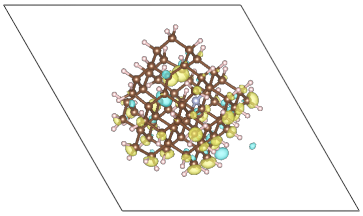

(b) $LUMO$ in the α-spin channel at 0.272 GPa.

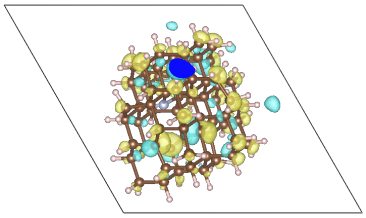

(c) $LUMO$ in the α-spin channel at 0.506 GPa.

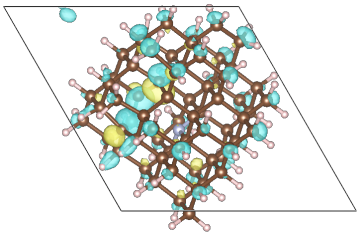

(d) $LUMO$ in the α-spin channel at 1.06 GPa.

Figure 6.10: LUMO wavefunctions shape stability increasing the pressure in $C_{67}H_{62}NV^{-}$.

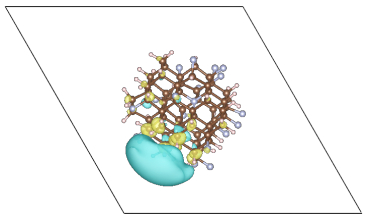

(a) $LUMO$ in the α-spin channel at 0.301 GPa.

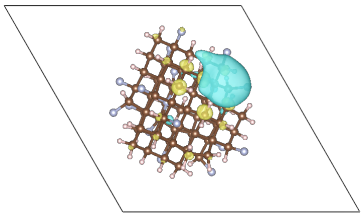

(b) $LUMO$ in the α-spin channel at 0.484 GPa.

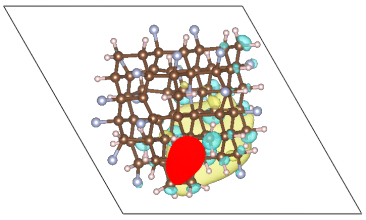

(c) $LUMO$ in the α-spin channel at 0.883 GPa.

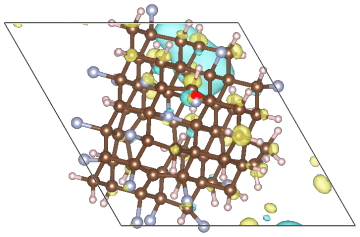

(d) $LUMO$ in the α-spin channel at 1.665 GPa.

Figure 6.11: LUMO wavefunctions shape stability increasing the pressure in $C_{67}H_{45}F_{17}NV^{-}$.

This evidence demonstrates even better why the energy increase phenomenon is related to the quantum confinement effect.

6.3. Electron-Phonon Renormalization

After having studied the effect of the pressure on the molecular crystal, we have decided to advance the description of our system including the electron-phonon interaction. As a consequence, it is possible to evaluate the effect of the temperature on the electronic structure of the system.
To perform the analysis, we have considered the most pressurized crystal since it was possible to obtain the results of the calculations within a reasonable amount of time.
In fact, it is necessary to stress that, to obtain reliable results, a wide number of displaced samples, has to be generated, and a DFT calculation has to be performed for each configuration.
In particular, in table 6.1, we report a preliminary analysis of the estimated computational time needed to obtain statistically meaningful electron-phonon renormalization results, based on the computational time needed to complete one single DFT calculation on each molecular crystal.

Pressure [GPa]	DFT single point [s]	Computational time
1.6654	250	3 days
0.8827	750	9 days
0.4836	1500	17 days
0.3005	4020	46 days
0.1989	7700	88 days

Table 6.1: Computational time needed to compute the electron-phonon renormalization for each pressure.

The total computational time in table 6.1 considers both the calculations needed to retrieve the dynamical matrix and the calculation of the significant statistical sample of 200 configurations.
All the DFT calculations performed in this analysis were carried out using Qbox, coupled with PyEPFD [30][31][1], a Python package that allows to create all the Qbox input files needed to compute the dynamical matrix, the phonon frequencies, and the electron-phonon renormalization following the approaches discussed in chapter 2.

6.3.1. Dynamical Matrix Calculation

As anticipated in the previous paragraph, the first important step is to obtain an accurate approximation of the dynamical matrix.
The dynamical matrix is computed by the finite displacement method, which consists of displacing each atom position along the Cartesian coordinates and generating for each displacement a Qbox input file. Then, DFT calculations on the created files are performed and, merging the results, it is possible to retrieve the potential energy surface around the ion equilibrium positions. Finally, it is possible to compute the dynamical matrix following the harmonic approximation. For the sake of detail, PyEPFD compute the dynamical matrix as the Jacobian matrix of the forces that act on each ion in the displaced coordinates, which is equivalent to evaluate it as the Hessian matrix of the potential energy.
The calculation of a precise dynamical matrix is dependent on the accuracy of the potential energy surface that is obtained, so it is important to evaluate which is the best possible way to scan that surface.
We have decided to evaluate the potential energy considering different displacement numbers for each coordinate, and different displacement amplitudes.
The results that we have obtained for each approach are reported in table 6.2.

# Displacement	1	2	4	2
Displacement [Å]	0.005	0.02	0.03	0.02
BFGS optimization (i-PI)	no	no	no	yes
Low-frequencies [cm^{-1}]	-35.8113	-23.5605	-18.2991	0.0000
	-0.0000	-0.0000	-9.0785	0.0000
	-0.0000	0.0000	-0.0000	0.0000
	0.0000	0.0000	-0.0000	26.6981
	7.0640	15.4943	-0.0000	37.5498
	33.2045	33.3588	29.6095	45.2681

Table 6.2: Dynamical matrix evaluation with the first six normal modes frequencies.

The quality of the dynamical matrix calculation can be retrieved by looking at the low-frequency modes: we expect to obtain only three zero-frequency modes, related to the crystal movement as a whole.
In the case of Qbox-optimized structures (10^{-5} $Ry/Bohr$), the frequencies suggest that we have not reached an accurate result for the potential energy surface scan, which could

be improved with a more refined optimization of the crystal structure.
For this reason, a trust-radius based BFGS optimization calculation was performed with i-PI [27], a universal force engine interface written in Python, designed to be used together with an ab initio, machine-learned, or force-field-based evaluation of the interactions between the atoms.
Additionally, we have considered to use also the results with the lower level of optimization, exploiting the PyEPFD capability of excluding the additional zero-frequency modes when the configurations sample is built. In this way, the divergence of the Bose-Einstein occupation factor (2.16) and of the Gaussian broadening (2.15) is avoided.
Now we can proceed to the second stage of the process: the evaluation of the electron-phonon renormalization.

6.3.2. Electron-Phonon Results

First of all, we have carried out calculations at $T = 0\ K$ to understand which are the issues related to the divergences, obtaining precious insight on the low-energy phonons effect. Additionally, we have explored the differences between two different algorithms for the generation of the configuration sample: the one-shot random with antithetic pair (OSRAP) and the Monte Carlo with antithetic pair (MCAP).
Within the dynamical matrices calculated on the Qbox-optimized structure, we have chosen the second in table 6.2 for the next analysis.

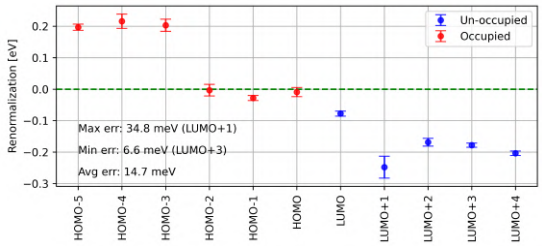

(a) Electron-phonon renormalization in the α-spin channel ($\omega_k > 30\ cm^{-1}$).

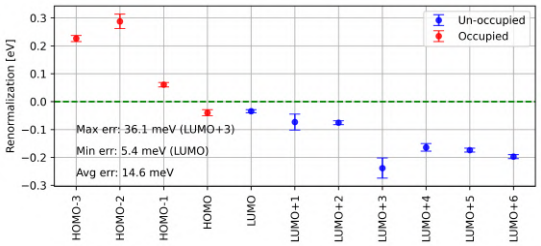

(b) Electron-phonon renormalization in the β-spin channel ($\omega_k > 30\ cm^{-1}$).

Figure 6.12: Electron-phonon renormalization obtained with the OSRAP algorithm and 600 independent confiugrations.

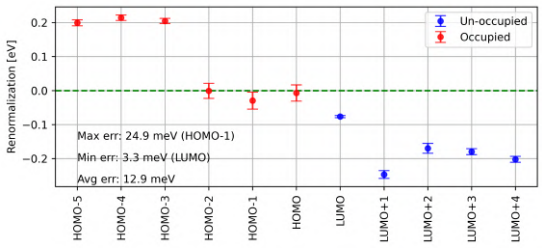

(a) Electron-phonon renormalization in the α-spin channel ($\omega_k > 30\ cm^{-1}$).

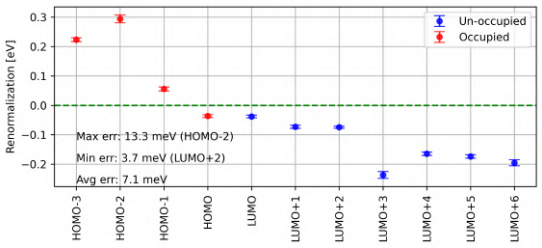

(b) Electron-phonon renormalization in the β-spin channel ($\omega_k > 30\ cm^{-1}$).

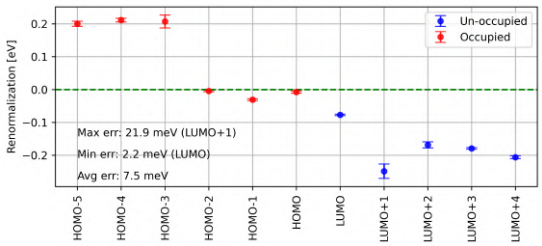

(c) Electron-phonon renormalization in the α-spin channel ($\omega_k > 35\ cm^{-1}$).

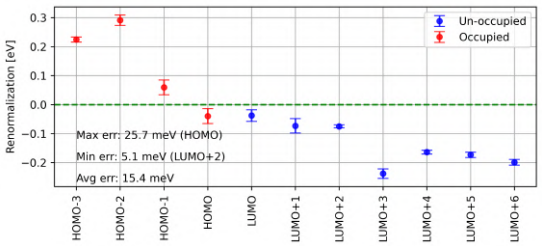

(d) Electron-phonon renormalization in the β-spin channel ($\omega_k > 35\ cm^{-1}$).

Figure 6.13: Electron-phonon renormalization obtained with the MCAP algorithm and 600 independent configurations.

Despite the OSRAP algorithm guarantees a faster convergence, the results are more accurate with the MCAP algorithm, which can even halve the maximum error in the electron-phonon renormalization predictions on the same statistical sample.
For this reason, we have decided to compute the electron-phonon renormalization on the i-PI optimized structure only with the MCAP algorithm.
Secondly, we can confirm that the low-frequency normal modes do not affect massively the accuracy of the results, in fact, excluding the frequencies below 35 cm^{-1}, the uncertainty does not improve significantly.
Moreover, we want to stress that the results obtained with the different approaches are almost identical, underlying the reliability of the electron-phonon renormalization results.

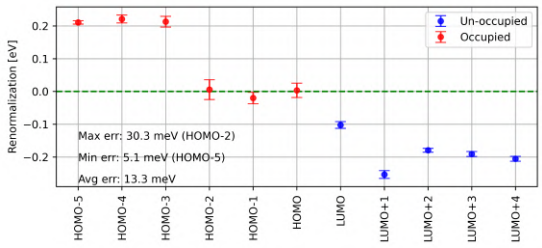

(a) Electron-phonon renormalization in the α-spin channel (no ω_k excluded).

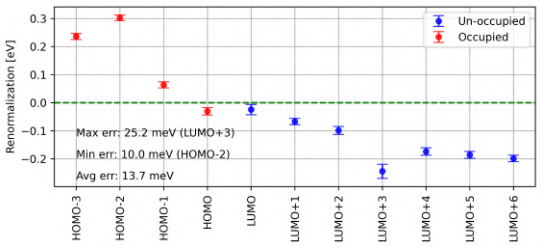

(b) Electron-phonon renormalization in the β-spin channel (no ω_k excluded).

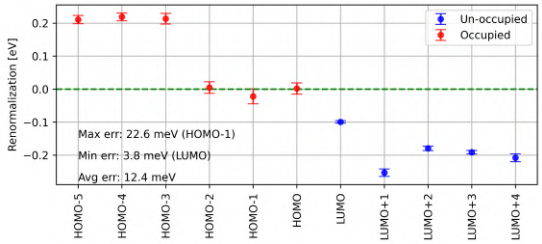

(c) Electron-phonon renormalization in the α-spin channel ($\omega_k > 40\ cm^{-1}$).

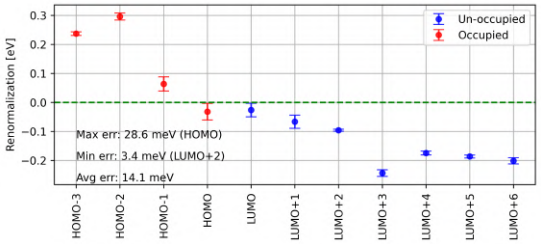

(d) Electron-phonon renormalization in the β-spin channel ($\omega_k > 40\ cm^{-1}$).

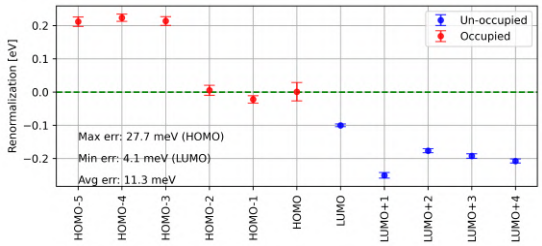

(e) Electron-phonon renormalization in the α-spin channel ($\omega_k > 46\ cm^{-1}$).

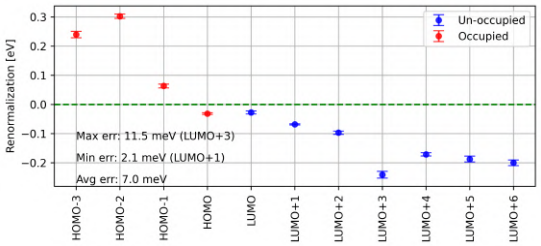

(f) Electron-phonon renormalization in the β-spin channel ($\omega_k > 46\ cm^{-1}$).

Figure 6.14: Electron-phonon renormalization on the i-PI optimized molecular crystal obtained with the MCAP algorithm and 600 independent configurations.

Nevertheless, after having taken all frequencies into account, the accuracy in the i-PI optimised case is sufficiently high and, as general consequence of the inclusion of low-frequency modes, we can find an increase in the maximum error.
Within the acquired accuracy, the magnitude of the electron-phonon renormalization does not change the electronic structure of the molecular crystal significantly (in figure 6.15) and confirms the system's promise for quantum information applications.
In particular, we can notice that, even if the gap is reduced, the defect levels are almost unaffected by the phonon coupling.

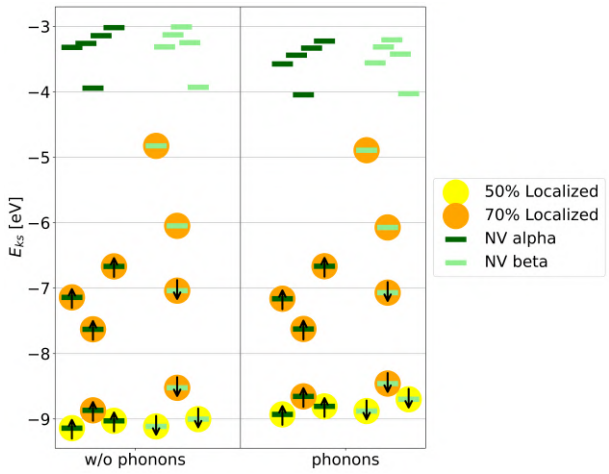

Figure 6.15: Electronic structures of the $C_{67}H_{45}F_{17}NV^{-}$ at 1.665 GPa when the electron-phonon interaction is considered.

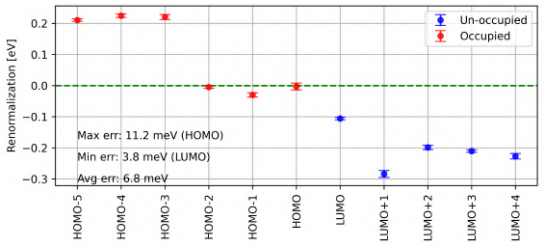

(a) Electron-phonon renormalization in the α-spin channel at 300 K (no ω_k excluded).

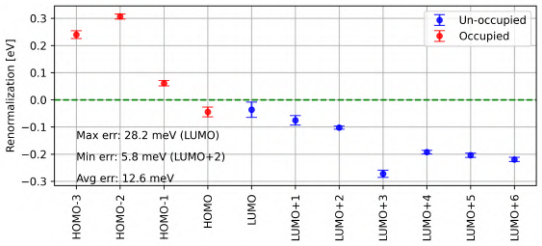

(b) Electron-phonon renormalization in the β-spin channel at 300 K (no ω_k excluded).

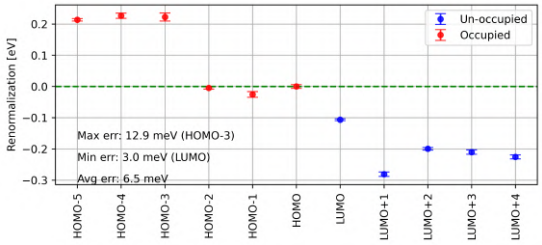

(c) Electron-phonon renormalization in the α-spin channel at 300 K ($\omega_k > 46\ cm^{-1}$).

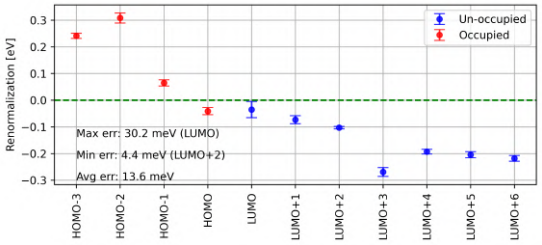

(d) Electron-phonon renormalization in the β-spin channel at 300 K ($\omega_k > 46\ cm^{-1}$).

Figure 6.16: Electron-phonon renormalization on the i-PI optimized molecular crystal obtained with the MCAP algorithm and 600 independent configurations at 300 K.

Then, we have chosen to assess the impact of the phonons on the molecular crystal electronic structure at room temperature ($T = 300\ K$), following the 0 K analysis.
The temperature increase does not affect the accuracy of the results, even if the maximum error increases in the beta spin channel (in figure 6.16).

From the perspective of stability, we observe in figure 6.17 that the electron-phonon coupling effect is advantageous since the NV electronic structure is maintained and the LUMO, along with all the other empty orbitals, is stabilized. The increase in the valence band energy is not detrimental because in the NV-diamond electronic structure the lower defect levels reside into the valence band, so we can assume also in this molecular system that the NV properties are not affected by this beahviour.
Moreover, if we compare the electron-phonon renormalization in figures 6.14 and 6.16, both with and without the frequency cut-off, the magnitude of the electron-phonon renormalization does not change with the temperature that reaches 300 K, underlining the insensitivity of the electronic structure of this system to large temperature variation. This is crucial to obtain an ambient-temperature reliable qubit system.

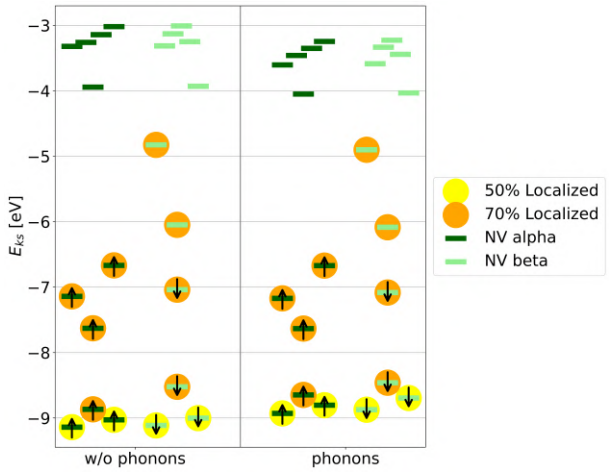

Figure 6.17: Electronic structures with the electron-phonon renormalization of the $C_{67}H_{45}F_{17}NV^{-}$ at 1.665 GPa and 300 K.

In this chapter, we explored the effect of pressure and temperature on nanodiamond molecular crystals, including the electron-phonon coupling.
The quantum confinement effect, caused by the increasing pressure, lifts the conduction band levels that are not completely localized on the nanoparticle, creating more space to accommodate the defect levels. This beneficial behavior is also coupled with an increasing localization of the defect levels in the vacancy.
When we introduced the effect of the temperature, including the electron-phonon interaction, we demonstrated that the molecular crystal at high pressure shows an electronic structure weakly dependent on the temperature, which is crucial for this qubit system.
These observations in the molecular crystal electronic structure emphasize the system's promise in the context of quantum information science application.

7 | Conclusions and Further Research

The central endeavor of this research was to scrutinize the suitability of distinct diamondoid systems when coupled with the nitrogen-vacancy (NV) center for quantum information science applications.
During the course of this theoretical and computational study, developed within the Density Functional Theory framework, we have unveiled several noteworthy findings.
Firstly, we have established that isolated H-terminated diamondoids, in which the NV-center is embedded, lack the presence of localized empty states below the vacuum level, thus rendering them inherently unsuitable as qubits since any optical control protocol is impossible to establish without letting escape the additional electron.
Conversely, once the surface was engineered, we have demonstrated that terminations involving hydroxyl (OH), thiol (SH), or carbonyl (CHO) groups offer the advantage of stabilizing nanodiamonds, guaranteeing a positive electronic affinity.
This effect stems from the electron-withdrawing nature of these functional groups.
However, it became apparent that these terminations do not exert a favorable influence on the NV-electronic structure, which is a requisite element for the realization of quantum information processing.

In contrast, we have revealed a promising direction through the exploration of fluorine termination.
This particular termination demonstrated the capability to effectuate a complete reconstruction of the NV electronic structure. In fact, this functionalization guarantees the presence of localized empty levels, which characterize a nanostructure with a positive electronic affinity, residing within the electronic band gap.
The emergence of such localized states within the band gap offers intriguing prospects for the manipulation of NV centers within diamondoids with the purpose of realizing reliable

and robust qubits.

Finally, we have analyzed the effects of pressure on diamondoid molecular crystals and we have also included the electron-phonon interaction, which allows also to account for the temperature effect on the electronic structure.
It emerged that pressure exerts a favorable influence from the perspective of practical applications since the increase in the gap guarantees a more spacious accommodation for the NV-levels. Given that, it is eventually possible to build more robust qubit manipulation protocols.
Moreover, we have found that the underlying mechanism facilitating this enhancement resides in the phenomenon of quantum confinement.
On the other hand, the gap is only slightly reduced by the electron-phonon renormalization, which is not harmful to the applications, even at room temperature.

This research endeavor contributes significantly to the understanding of the electronic properties of diamondoids in the context of quantum technologies. Nevertheless, it is imperative to acknowledge the existence of certain limitations inherent to this study, including the constraints imposed by the extreme computational demand needed for each calculation, that limited the possibility of exploring deeply some of the analyzed systems. Furthermore, it has to be reminded that none of these systems has been already produced, but the encouraging experimental works cited in the bibliography have shown the probable capability to produce the most promising structures [36, 53].
On the other hand, the exploitation of plane waves basis set properties gave the opportunity to obtain precise references and accurate results, at the expense of the computational time needed. Moreover, in this framework, it was possible to investigate rigorously the effect of pressure on the diamondoid molecular crystal, which would not be practicable at the same level of precision with other basis sets implied.
In light of this, the implications arising from these numerical findings hold promising significance within the domain of quantum information science, giving a direction to follow for eventual experimental realizations.

7.1. Recommendations and Future Directions

In this section, several promising avenues are outlined for future research and experimentation. These recommendations are designed to build upon the findings of this study and

further advance the understanding of diamondoid-based quantum systems for practical applications.

7.1.1. Experimental Measurement

The first interesting aspect that could be investigated is the experimental realization and characterization of the systems that are analyzed in this work.
Experimentation provides a crucial bridge between theoretical predictions and practical applications.
Experimental setups should involve the synthesis of F-terminated diamondoids and the creation of NV center configurations with controlled parameters. Characterization techniques, such as electron spin resonance (ESR) spectroscopy and photoluminescence measurements, can be employed to probe the electronic and optical properties of these systems.
In particular, ESR spectroscopy can provide valuable insights into the electron spin dynamics and the presence of localized empty states.
Photoluminescence measurements can shed light on the quantum emission properties of F-terminated diamondoids with NV centers, offering a direct assessment of their potential for quantum information processing and sensing.

7.1.2. Decoherence Time Simulation

Decoherence represents a critical challenge in quantum information processing. To harness the full potential of NV centers embedded in F-terminated diamondoids, it is imperative to investigate and eventually consider how to mitigate decoherence effects.
In particular, to tackle these latter eventual effects it would be necessary to understand which is the dominating decoherence mechanism, considering the spin-phonons interaction and the interaction with all the other nuclear spin in the nanoparticle. [35]
This would also reveal eventual possibilities and difficulties in storing information and entangling adjacent qubits in real devices.

7.1.3. Post-DFT Calculation

While density functional theory (DFT) has been a valuable tool in understanding the electronic properties of diamondoids, post-DFT calculations offer a pathway to refine our models and predictions.
Post-DFT methods, such as many-body perturbation theory (MBPT), quantum Monte

Carlo (QMC), and complete active space self-consistent field (CASSCF), can provide more accurate descriptions of electronic correlations and excitations.
In fact, it was demonstrated the incredible accuracy of this methods in predicting the experimentally measured NV-center electronic structure, overcoming all the calculation bias introduced by DFT.
Incorporating post-DFT calculations into this research can lead to a more comprehensive understanding of the electronic structure of F-terminated diamondoids with NV centers. These calculations can yield insights into excited states and electron correlation effects.

In summary, this research has shed light on the electronic properties of the NV-center embedded in isolated diamondoids and diamondoid molecular crystals within the context of quantum information science. These findings, when combined with future research efforts in this field, have the potential to advance the discipline, contributing to progress in quantum technology.

Bibliography

[1] Pyepfd website. https://pyepfd.readthedocs.io/en/.

[2] J. Ackermann and A. Krueger. Efficient surface functionalization of detonation nanodiamond using ozone under ambient conditions. *Nanoscale*, 11:8012–8019, 2019. doi: 10.1039/C9NR01716J. URL http://dx.doi.org/10.1039/C9NR01716J.

[3] C. Adamo and V. Barone. Toward reliable density functional methods without adjustable parameters: The PBE0 model. *The Journal of Chemical Physics*, 110 (13):6158–6170, 04 1999. ISSN 0021-9606. doi: 10.1063/1.478522. URL https://doi.org/10.1063/1.478522.

[4] D. G. M. Anderson. Iterative procedures for nonlinear integral equations. *J. ACM*, 12:547–560, 1965. URL https://api.semanticscholar.org/CorpusID:202156.

[5] F. Arute, K. Arya, R. Babbush, D. Bacon, J. C. Bardin, R. Barends, R. Biswas, S. Boixo, F. G. S. L. Brandao, D. A. Buell, B. Burkett, Y. Chen, Z. Chen, B. Chiaro, R. Collins, W. Courtney, A. Dunsworth, E. Farhi, B. Foxen, A. Fowler, C. Gidney, M. Giustina, R. Graff, K. Guerin, S. Habegger, M. P. Harrigan, M. J. Hartmann, A. Ho, M. Hoffmann, T. Huang, T. S. Humble, S. V. Isakov, E. Jeffrey, Z. Jiang, D. Kafri, K. Kechedzhi, J. Kelly, P. V. Klimov, S. Knysh, A. Korotkov, F. Kostritsa, D. Landhuis, M. Lindmark, E. Lucero, D. Lyakh, S. Mandrà, J. R. McClean, M. McEwen, A. Megrant, X. Mi, K. Michielsen, M. Mohseni, J. Mutus, O. Naaman, M. Neeley, C. Neill, M. Y. Niu, E. Ostby, A. Petukhov, J. C. Platt, C. Quintana, E. G. Rieffel, P. Roushan, N. C. Rubin, D. Sank, K. J. Satzinger, V. Smelyanskiy, K. J. Sung, M. D. Trevithick, A. Vainsencher, B. Villalonga, T. White, Z. J. Yao, P. Yeh, A. Zalcman, H. Neven, and J. M. Martinis. Quantum supremacy using a programmable superconducting processor. *Nature*, 574(7779):505–510, Oct. 2019.

[6] S. L. Bayliss, P. Deb, D. W. Laorenza, M. Onizhuk, G. Galli, D. E. Freedman, and D. D. Awschalom. Enhancing spin coherence in optically addressable molecular qubits through host-matrix control. *Phys. Rev. X*, 12:031028, Aug 2022. doi: 10.

1103/PhysRevX.12.031028. URL https://link.aps.org/doi/10.1103/PhysRevX.12.031028.

[7] A. Becke. Density-functional thermochemistry. iii. the role of exact exchange. j. chem. phys., 98: 5648-5652, 1993.

[8] A. Boretti, L. Rosa, J. Blackledge, and S. Castelletto. Nitrogen-vacancy centers in diamond for nanoscale magnetic resonance imaging applications. *Beilstein J. Nanotechnol.*, 10:2128–2151, Nov. 2019.

[9] K. R. Brown, J. Chiaverini, J. M. Sage, and H. Häffner. Materials challenges for trapped-ion quantum computers. *Nature Reviews Materials*, 6(10):892–905, Oct. 2021.

[10] E. H. Chen, H. A. Clevenson, K. A. Johnson, L. M. Pham, D. R. Englund, P. R. Hemmer, and D. A. Braje. High-sensitivity spin-based electrometry with an ensemble of nitrogen-vacancy centers in diamond. *Phys. Rev. A*, 95:053417, May 2017. doi: 10.1103/PhysRevA.95.053417. URL https://link.aps.org/doi/10.1103/PhysRevA.95.053417.

[11] A. A. Correa, S. A. Bonev, and G. Galli. Carbon under extreme conditions: Phase boundaries and electronic properties from first-principles theory. *Proceedings of the National Academy of Sciences*, 103(5):1204–1208, 2006. doi: 10.1073/pnas.0510489103. URL https://www.pnas.org/doi/abs/10.1073/pnas.0510489103.

[12] D. P. DiVincenzo. The physical implementation of quantum computation. *Fortschritte der Physik*, 48(9-11):771–783, sep 2000. doi: 10.1002/1521-3978(200009)48:9/11<771::aid-prop771>3.0.co;2-e. URL https://doi.org/10.1002%2F1521-3978%28200009%2948%3A9%2F11%3C771%3A%3Aaid-prop771%3E3.0.co%3B2-e.

[13] M. W. Doherty, N. B. Manson, P. Delaney, F. Jelezko, J. Wrachtrup, and L. C. Hollenberg. The nitrogen-vacancy colour centre in diamond. *Physics Reports*, 528(1):1–45, 2013. ISSN 0370-1573. doi: https://doi.org/10.1016/j.physrep.2013.02.001. URL https://www.sciencedirect.com/science/article/pii/S0370157313000562. The nitrogen-vacancy colour centre in diamond.

[14] S. Fredericks, K. Parrish, D. Sayre, and Q. Zhu. Pyxtal: A python library for crystal structure generation and symmetry analysis. *Computer Physics Communications*, 261:107810, 2021. ISSN 0010-4655. doi: https://doi.org/10.1016/j.cpc.2020.107810. URL https://www.sciencedirect.com/science/article/pii/S0010465520304057.

[15] G. Galli. *Structure, Stability and Electronic Properties of Nanodiamonds*, pages 37–56. Springer Netherlands, Dordrecht, 2010. ISBN 978-1-4020-9718-8. doi: 10.1007/978-1-4020-9718-8_2. URL https://doi.org/10.1007/978-1-4020-9718-8_2.

[16] P. García-Risueño, P. Han, S. Kumar, and G. Bester. Frozen-phonon method for state anticrossing situations and its application to zero-point motion effects in diamondoids. *Phys. Rev. B*, 108:125403, Sep 2023. doi: 10.1103/PhysRevB.108.125403. URL https://link.aps.org/doi/10.1103/PhysRevB.108.125403.

[17] M. Govoni and G. Galli. Gw100: Comparison of methods and accuracy of results obtained with the west code. *Journal of Chemical Theory and Computation*, 14(4): 1895–1909, 2018. doi: 10.1021/acs.jctc.7b00952. URL https://doi.org/10.1021/acs.jctc.7b00952. PMID: 29397712.

[18] L. K. Grover. A fast quantum mechanical algorithm for database search, 1996.

[19] F. Gygi. Architecture of qbox: A scalable first-principles molecular dynamics code. *IBM J. Res. Dev.*, 52(1/2):137–144, jan 2008. ISSN 0018-8646.

[20] M. Hanwell, D. Curtis, D. Lonie, T. Vandermeersch, E. Zurek, and G. Hutchison. Avogadro: An advanced semantic chemical editor, visualization, and analysis platform. *Journal of Cheminformatics*, 2012.

[21] J. Heyd, G. E. Scuseria, and M. Ernzerhof. Hybrid functionals based on a screened Coulomb potential. *The Journal of Chemical Physics*, 118(18):8207–8215, 04 2003. ISSN 0021-9606. doi: 10.1063/1.1564060. URL https://doi.org/10.1063/1.1564060.

[22] M. Hochstenbach and Y. Notay. The jacobi–davidson method. *GAMM-Mitteilungen*, 29(2):368–382, 2006. doi: https://doi.org/10.1002/gamm.201490038. URL https://onlinelibrary.wiley.com/doi/abs/10.1002/gamm.201490038.

[23] S. Ishii, S. Saiki, S. Onoda, Y. Masuyama, H. Abe, and T. Ohshima. Ensemble negatively-charged nitrogen-vacancy centers in type-ib diamond created by high fluence electron beam irradiation. *Quantum Beam Science*, 6(1), 2022. ISSN 2412-382X. doi: 10.3390/qubs6010002. URL https://www.mdpi.com/2412-382X/6/1/2.

[24] J. Johansson, P. Nation, and F. Nori. Qutip: An open-source python framework for the dynamics of open quantum systems. *Computer Physics Communications*, 183(8):1760–1772, 2012. ISSN 0010-4655. doi: https://doi.org/10.1016/j.cpc.2012.02.021. URL https://www.sciencedirect.com/science/article/pii/S0010465512000835.

[25] R. Johnson. Computational chemistry comparison and benchmark database http://cccbdb.nist.gov/ doi:10.18434/t47c7z. 04 2018. doi: 10.18434/T47C7Z.

[26] I. Joseph, Y. Shi, M. D. Porter, A. R. Castelli, V. I. Geyko, F. R. Graziani, S. B. Libby, and J. L. DuBois. Quantum computing for fusion energy science applications. *Physics of Plasmas*, 30(1):010501, 01 2023. ISSN 1070-664X. doi: 10.1063/5.0123765. URL `https://doi.org/10.1063/5.0123765`.

[27] V. Kapil, M. Rossi, O. Marsalek, R. Petraglia, Y. Litman, T. Spura, B. Cheng, A. Cuzzocrea, R. H. Meißner, D. M. Wilkins, B. A. Helfrecht, P. Juda, S. P. Bienvenue, W. Fang, J. Kessler, I. Poltavsky, S. Vandenbrande, J. Wieme, C. Corminboeuf, T. D. Kühne, D. E. Manolopoulos, T. E. Markland, J. O. Richardson, A. Tkatchenko, G. A. Tribello, V. Van Speybroeck, and M. Ceriotti. i-pi 2.0: A universal force engine for advanced molecular simulations. *Computer Physics Communications*, 236:214–223, 2019. ISSN 0010-4655. doi: https://doi.org/10.1016/j.cpc.2018.09.020. URL `https://www.sciencedirect.com/science/article/pii/S0010465518303436`.

[28] A. Ketterer. *Modular variables in quantum information*. PhD thesis, 10 2016.

[29] W. Kohn and L. J. Sham. Self-consistent equations including exchange and correlation effects. *Phys. Rev.*, 140:A1133–A1138, Nov 1965. doi: 10.1103/PhysRev.140.A1133. URL `https://link.aps.org/doi/10.1103/PhysRev.140.A1133`.

[30] A. Kundu and G. Galli. Quantum vibronic effects on the electronic properties of molecular crystals. *J Chem Theory Comput*, 19(13):4011–4022, June 2023.

[31] A. Kundu, M. Govoni, H. Yang, M. Ceriotti, F. Gygi, and G. Galli. Quantum vibronic effects on the electronic properties of solid and molecular carbon. *Phys. Rev. Mater.*, 5:L070801, Jul 2021. doi: 10.1103/PhysRevMaterials.5.L070801. URL `https://link.aps.org/doi/10.1103/PhysRevMaterials.5.L070801`.

[32] A. Kundu, Y. Song, and G. Galli. Influence of nuclear quantum effects on the electronic properties of amorphous carbon. *Proceedings of the National Academy of Sciences*, 119(31):e2203083119, 2022. doi: 10.1073/pnas.2203083119. URL `https://www.pnas.org/doi/abs/10.1073/pnas.2203083119`.

[33] C. Laube, R. Temme, A. Prager, J. Griebel, W. Knolle, and B. Abel. Fluorescence lifetime control of nitrogen vacancy centers in nanodiamonds for Long-Term information storage. *ACS Nano*, 17(16):15401–15410, Aug. 2023.

[34] X. Liu, L. Li, Q. Li, Y. Li, and F. Lu. Optical and mechanical properties of c, si, ge, and 3c–sic determined by first-principles theory using heyd–scuseria–ernzerhof

functional. *Materials Science in Semiconductor Processing*, 16(6):1369–1376, 2013. ISSN 1369-8001. doi: https://doi.org/10.1016/j.mssp.2013.04.017. URL https://www.sciencedirect.com/science/article/pii/S1369800113001212.

[35] A. Lunghi. *Spin-Phonon Relaxation in Magnetic Molecules: Theory, Predictions and Insights*, pages 219–289. Springer International Publishing, Cham, 2023. ISBN 978-3-031-31038-6. doi: 10.1007/978-3-031-31038-6_6. URL https://doi.org/10.1007/978-3-031-31038-6_6.

[36] Z. Luo, Q. Wan, Z. Yu, S. Lin, Z. Xie, and X. Wang. Photo-fluorination of nanodiamonds catalyzing oxidative dehydrogenation reaction of ethylbenzene. *Nature Communications*, 12(1):6542, Nov. 2021.

[37] G. Makov and M. C. Payne. Periodic boundary conditions in ab initio calculations. *Phys. Rev. B*, 51:4014–4022, Feb 1995. doi: 10.1103/PhysRevB.51.4014. URL https://link.aps.org/doi/10.1103/PhysRevB.51.4014.

[38] R. M. Martin. *Electronic Structure: Basic Theory and Practical Methods*. Cambridge University Press, 2004. doi: 10.1017/CBO9780511805769.

[39] N. Marzari, A. A. Mostofi, J. R. Yates, I. Souza, and D. Vanderbilt. Maximally localized wannier functions: Theory and applications. *Rev. Mod. Phys.*, 84:1419–1475, Oct 2012. doi: 10.1103/RevModPhys.84.1419. URL https://link.aps.org/doi/10.1103/RevModPhys.84.1419.

[40] K. Momma and F. Izumi. *VESTA*: a three-dimensional visualization system for electronic and structural analysis. *Journal of Applied Crystallography*, 41(3):653–658, Jun 2008. doi: 10.1107/S0021889808012016. URL https://doi.org/10.1107/S0021889808012016.

[41] Y. Peng, C. Cai, C. Fang, L. Wu, J. Liu, P. Sun, and D. Liu. Diamondoids and thiadiamondoids generated from hydrothermal pyrolysis of crude oil and TSR experiments. *Scientific Reports*, 12(1):196, Jan. 2022.

[42] J. P. Perdew, K. Burke, and M. Ernzerhof. Generalized gradient approximation made simple. *Phys. Rev. Lett.*, 77:3865–3868, Oct 1996. doi: 10.1103/PhysRevLett.77.3865. URL https://link.aps.org/doi/10.1103/PhysRevLett.77.3865.

[43] A. Petrone, J. J. Goings, and X. Li. Quantum confinement effects on optical transitions in nanodiamonds containing nitrogen vacancies. *Phys. Rev. B*, 94:165402, Oct 2016. doi: 10.1103/PhysRevB.94.165402. URL https://link.aps.org/doi/10.1103/PhysRevB.94.165402.

[44] A. Savvin, A. Dormidonov, E. Smetanina, V. Mitrokhin, E. Lipatov, D. Genin, S. Potanin, A. Yelisseyev, and V. Vins. NV– diamond laser. *Nature Communications*, 12(1):7118, Dec. 2021.

[45] N. Sheng, C. Vorwerk, M. Govoni, and G. Galli. Green's function formulation of quantum defect embedding theory. *Journal of Chemical Theory and Computation*, 18(6):3512–3522, 2022. doi: 10.1021/acs.jctc.2c00240. URL https://doi.org/10.1021/acs.jctc.2c00240. PMID: 35648660.

[46] F. Shi, X. Rong, N. Xu, Y. Wang, J. Wu, B. Chong, X. Peng, J. Kniepert, R.-S. Schoenfeld, W. Harneit, M. Feng, and J. Du. Room-temperature implementation of the deutsch-jozsa algorithm with a single electronic spin in diamond. *Physical Review Letters*, 105(4), jul 2010. doi: 10.1103/physrevlett.105.040504. URL https://doi.org/10.1103%2Fphysrevlett.105.040504.

[47] P. W. Shor. Polynomial-time algorithms for prime factorization and discrete logarithms on a quantum computer. *SIAM Journal on Computing*, 26(5):1484–1509, oct 1997. doi: 10.1137/s0097539795293172. URL https://doi.org/10.1137%2Fs0097539795293172.

[48] J. Sun, R. Remsing, Y. Zhang, Z. Sun, A. Ruzsinszky, H. Peng, Z. Yang, A. Paul, U. Waghmare, W. Xifan, M. Klein, and J. Perdew. Scan: An efficient density functional yielding accurate structures and energies of diversely-bonded materials. 11 2015.

[49] J. Sun, A. Ruzsinszky, and J. P. Perdew. Strongly constrained and appropriately normed semilocal density functional. *Phys. Rev. Lett.*, 115:036402, Jul 2015. doi: 10.1103/PhysRevLett.115.036402. URL https://link.aps.org/doi/10.1103/PhysRevLett.115.036402.

[50] J. Višňák. Quantum algorithms for computational nuclear physics. In *European Physical Journal Web of Conferences*, volume 100 of *European Physical Journal Web of Conferences*, page 01008, July 2015. doi: 10.1051/epjconf/201510001008.

[51] Y. Wu, Y. Wang, X. Qin, X. Rong, and J. Du. A programmable two-qubit solid-state quantum processor under ambient conditions. *npj Quantum Information*, 5(1):9, Jan. 2019.

[52] F. Yang, Y. Lin, M. Baldini, J. E. P. Dahl, R. M. K. Carlson, and W. L. Mao. Effects of molecular geometry on the properties of compressed diamondoid crystals. *Journal of Physical Chemistry Letters*, 7(22), 11 2016. doi: 10.1021/acs.jpclett.6b02161.

[53] R. Ye, X. Han, D. V. Kosynkin, Y. Li, C. Zhang, B. Jiang, A. A. Martí, and J. M. Tour. Laser-Induced conversion of teflon into fluorinated nanodiamonds or fluorinated graphene. *ACS Nano*, 12(2):1083–1088, Feb. 2018.

[54] Ádám Gali. Ab initio theory of the nitrogen-vacancy center in diamond. *Nanophotonics*, 8(11):1907–1943, 2019. doi: doi:10.1515/nanoph-2019-0154. URL `https://doi.org/10.1515/nanoph-2019-0154`.

List of Figures

List of Tables